Energy 366 (2026) 142785

Contents lists available at ScienceDirect

Energy

journal homepage: www.elsevier.com/locate/energy

Numerical study of heat extraction from an enhanced geothermal system combined with closed coaxial heat exchangers in complex fractured reservoirs

Guoying Wang [a,b], Guofeng Song [c,*], Housheng Jia [a,b,**], Hongwei Ma [a], Lei Wang [d], Norbert Klitzsch [e], Shaowei Liu [a,b], Gan Feng [f], Chuanliang Yan [g], Zhazha Hu [a,b]

[a] School of Energy Science and Engineering, Henan Polytechnic University, Jiaozuo, 454002, China
[b] State Collaborative Innovation Center of Coal Work Safety and Clean-efficiency Utilization, Henan Polytechnic University, Jiaozuo, 454002, China
[c] Department of Geoscience and Engineering, Delft University of Technology, Delft, 2628CN, the Netherlands
[d] Key Laboratory of In-situ Property-improving Mining of Ministry of Education, Taiyuan University of Technology, Taiyuan, 030024, China
[e] Institute for Applied: Geophysics' and Geothermal Energy, RWTH Aachen University, 52074, Aachen, Germany
[f] State Key Laboratory of Hydraulics and Mountain River Engineering, College of Water Resource &Hydropower, Sichuan University, Chengdu, 610065, China
[g] Key Laboratory of Unconventional Oil & Gas Development (China University of Petroleum (East China)), Ministry of Education, China

ARTICLE INFO

Keywords:
Hot dry rock
Enhanced geothermal system
Coaxial heat exchangers
Complex fractured geothermal reservoir
Heat extraction performance

ABSTRACT

This study proposes an innovative geothermal exploration system that combines an enhanced geothermal system (EGS) and a closed coaxial heat exchanger geothermal system (CCGS) for heat extraction in discrete fracture networks and coaxial wells. Firstly, a mathematical model was established, considering the fluid flow and heat transfer processes in fractures, reservoir matrix, and wellbores. Subsequently, an analysis was conducted to examine the temperature and velocity contours in discrete fracture networks and coaxial wells. Moreover, the heat extraction performance of the proposed EGS-CCGS was compared with that of a traditional EGS. Finally, the key factors affecting heat production were discussed and analyzed. The results showed that the CCGS can significantly enhance the heat extraction efficiency of fractured geothermal systems. When fracture connectivity is suboptimal, the heat extraction efficiency for the system can be improved by up to 150%. The optimal injection rates for the combined EGS-CCGS system are 120 kg/s for the EGS and 25 kg/s for the CCGS. When the fracture connectivity is low, the rock matrix thermal conductivity has a significant impact on heat extraction efficiency, while the fracture permeability has a relatively minor effect. Conversely, the opposite effects are reported when the fracture connectivity is high.

1. Introduction

Geothermal resources are distinguished by their clean and stable operation and wide spatial distribution. As a result, they have constituted a pivotal research and development subject over recent decades, serving as a promising alternative energy resource in countries worldwide [1]. To date, hydrothermal geothermal resources have been the primary focus of exploitation in many countries. However, a substantially larger proportion of geothermal energy reserves exists in hot dry rocks (HDR) formations, typically buried at depths of 3-10 km. These hot dry rocks feature a temperature range of 150-650°C and contain potential energy equivalent to 30 times the combined energy of all global reserves of oil, natural gas, and coal [2,3]. Despite this potential, HDR resource development remains largely confined to experimental research and pilot-scale field tests, with no large-scale commercial applications in operation [4,5]. Therefore, developing efficient approaches for harnessing heat from hot dry rock is essential for enabling its commercial exploitation.

Furthermore, the enhanced geothermal system (EGS) and deep borehole heat exchange (DBHE) [6,7] are widely regarded as the main methods of HDR exploitation across a range of applications. EGS refers to an engineered geothermal system in which an artificial reservoir is created within the deep, low-permeability HDR matrix through hydraulic fracturing, thereby enabling the long-term and economically

* Corresponding author.
** Corresponding author. School of Energy Science and Engineering, Henan Polytechnic University, Jiaozuo, 454002, China.
E-mail addresses: g.song-1@tudelft.nl (G. Song), jiahousheng@126.com (H. Jia).

https://doi.org/10.1016/j.energy.2026.142785
Received 30 March 2026; Received in revised form 12 October 2026; Accepted 15 October 2026
Available online 15 October 2026
0360-5442/© 2026 The Authors. Published by Elsevier Ltd. This is an open access article under the CC BY license (http://creativecommons.org/licenses/by/4.0/).

viable extraction of thermal energy [8]. A number of field experiments and numerical studies have been developed to examine the performance of EGS in hot dry rock systems. Field experiments at over 60 geothermal sites reveal three key challenges: (i) uncontrollable fracture extension, (ii) difficulty in connecting injection and production wells, and (iii) complex stress disturbances during HDR reservoir transformation. On this basis, the prediction of hydraulic fracture expansions under the combined influence of significant temperature differences, thermal stress, and natural fractures is very challenging [9,10]. For instance, the Fenton Hill project in the United States required 8 drilling and 5 fracturing operations over three stages of reservoir construction to realize power generation. However, the project was ultimately forced to terminate due to poor connectivity between induced fractures and wells, and the severe loss of circulation fluids [11]. Similar difficulties were encountered in the Rosemanowes project in the UK and the Hijiori HDR project in Japan, which encountered issues related to the missing connection between injection and production wells [12]. In the case of the Cooper Basin EGS project in Australia, four deep wells were drilled, with temperatures reaching 244°C at 4000 m depth, and extensive fracture networks were generated via hydraulic fracturing. Nevertheless, microseismic monitoring revealed that these fractures lacked interconnection, preventing effective fluid flow between wells [13]. HDR stimulation often produces numerous isolated fractures that do not contribute to efficient heat exchange, yet limited numerical research has addressed strategies for harnessing these disconnected fracture networks.

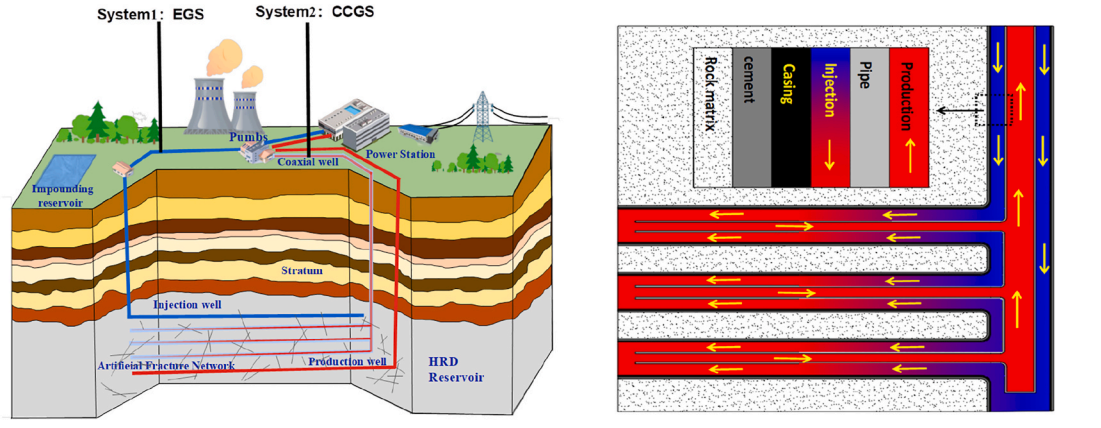
In examining DBHE methods for geothermal energy extraction from HDR formations, numerous numerical simulation studies have been performed to assess the heat extraction performance of coaxial borehole well heat exchangers (CBHE) and U-shaped deep well heat exchangers (UBHE). Wang et al. [14] comparatively evaluated the thermal performance of various CBHE configurations, reporting a maximum outlet temperature of 100.01°C. Sun et al. [15] investigated a UBHE system at a burial depth of 5000 m with a bottom-hole temperature of 183°C, yielding an outlet temperature of 77°C. Wang et al. [16] proposed a multi-level, multi-branch U-shaped well geothermal extraction method and conducted numerical research. The study found that the heat transfer efficiency is highest when the length of the horizontal well is 2000 m and the injection rate is 40 kg/s, with an outlet temperature of 130°C. Overall, these investigations highlight that the DBHE system's limited heat exchange area results in a relatively low outlet temperature, which in turn restricts the efficiency of the extraction of HDR resources.

Obviously, utilization of enhanced geothermal systems is confronted with challenges, including issues such as fracture closure, fluid short-circuiting, and inadequate fracture connectivity. These limitations result in a substantial proportion of induced fractures remaining underutilized as effective heat exchange interfaces between the working fluid and the HDR matrix. Furthermore, the outlet temperature of most deep-borehole heat exchanger (DBHE) systems is generally much lower than that of EGS. Therefore, a hybrid geothermal system is needed to utilize the disconnected fractures generated during EGS stimulation while improving the inherently low heat-extraction efficiency of DBHE systems.

Therefore, this study proposes a novel hybrid geothermal system that integrates an EGS with a closed coaxial geothermal system (CCGS), as illustrated in Fig. 1. In the EGS component, fluid circulates through hydraulically connected fractures to extract heat from the hot dry rock (HDR). In parallel, the CCGS component uses a downhole coaxial heat exchanger to recover heat directly from the surrounding rock through a closed-loop circulation system. Compared with a conventional EGS, the proposed EGS-CCGS system offers three main advantages: (i) it effectively extracts heat through hydraulically connected fractures; (ii) it recovers heat from the rock matrix surrounding poorly connected or isolated fractures without requiring fluid circulation through these fractures; and (iii) it combines fracture-based heat extraction through the EGS with direct heat extraction from the surrounding rock matrix through the DBHE, thereby improving the overall heat-recovery efficiency of the HDR reservoir.

Most current hybrid geothermal systems focus on integrating shallow geothermal resources with solar or biomass energy to enhance thermal quality, rather than optimizing system design to maximize heat extraction from deep high-temperature rock masses [17]. Some researchers have proposed well configurations (e.g., U-shaped or coaxial wells) for deep geothermal co-development. For example, Agson et al. [18] introduced a coaxial open-loop well design combined with controlled fracturing to reduce drilling costs, yet the system did not address heat extraction from unconnected fracture zones. Similarly, Gao et al. [19] utilized localized fracture networks to improve the thermal performance of coaxial borehole heat exchangers (CBHE), demonstrating higher efficiency than standalone CBHE systems. However, their approach assumed pre-existing fracture connectivity and overlooked fracture discontinuity as well as methods to harness heat from isolated rock masses. It is necessary to explore the synergistic integration of EGS and CCGS technologies to enable comprehensive utilization of HDR resources.

The proposed EGS-CCGS system thus represents a novel and potentially more effective pathway for large-scale, long-term geothermal energy recovery from deep HDR formations. To address the issues of insufficient connectivity in fracture networks, which leads to inefficient heat extraction from large volumes of HDR reservoirs, a novel combined EGS-CCGS system for complex fractured geothermal reservoirs is proposed. A 3D mathematical model incorporating seepage and heat



(a) Combined EGS-CCGS (b) Amplified schematic diagram of the CCGS system

Fig. 1. Schematic diagram of the combined EGS-CCGS system.

transfer in fractures, reservoir matrix, and coaxial wellbores is established. Then, an integrated system is constructed, comprising a 3D reservoir matrix, 2D fracture networks, and 1D wellbores, thereby forming the EGS-CCGS co-development system. Subsequently, the performance of the proposed system is then compared and analyzed against that of a conventional EGS. Thirdly, the effects of injection flow rate, horizontal well length, and hydraulic fracture number on heat extraction are analyzed. Finally, the economic feasibility of combined EGS-CCGS under various factors is examined.

2. Mathematical model

2.1. Model assumptions

In order to model the heat transfer behavior of EGS-CCGS systems in fractured reservoirs in a computationally efficient and stable manner, the following simplifying assumptions are employed:

(1) The reservoir consists of a discrete fracture network and a rock matrix, both modeled as continuous porous media. In practical HDR reservoirs, hydraulic stimulation commonly activates and connects pre-existing natural fractures. Therefore, the DFN adopted in this study represents the effective stimulated fracture network responsible for fluid flow and heat transfer, regardless of the specific geological origin of individual fractures.
(2) Fractures are modeled as two-dimensional elements, whereas wellbores are represented as one-dimensional elements
(3) Two one-dimensional element borehole model were established, one model represents the outer pipe of the coaxial well, and one model represents the inner pipe.
(4) In the same one-dimensional line element, the wall thickness of the wellbore is uniform, and the calculation process is automatically incorporated into the wall thickness calculation.
(5) The matrix permeability (10^{-18} m^2) is much lower than the fracture permeability (about 10^{-12} m^2), so the rock matrix can be considered nearly impermeable [20].
(6) The temperatures of the fluid and the rock matrix in discrete fractures are balanced using a local thermal equilibrium method [21,22]. The fluid and rock temperatures within each computational element are therefore described using a single effective temperature.
(7) The permeability of fractures is characterized as a function of temperature [23].

$$k = 2.8567 \times 10^{\left(-2.67\times10^{-3}T\right)} \tag{1}$$

where k is the permeability of fracture (mD), T is the temperature (^oC)

(8) The potential influence of proppants on fracture permeability and porosity has not been considered [19].
(9) Phase transition effects are not considered in the present model. Given that the simulated conditions (T < 300°C, P > 39.2 MPa) ensure a liquid state according to the IAPWS-IF97 formulation [24], the fluid is treated using liquid-phase thermophysical properties:

$$\rho_f = \begin{cases} 1000 \times \left(1 - \dfrac{\left(T_f - 3.98\right)^2}{503570} \times \dfrac{T_f + 283}{T_f + 67.26}\right) & 0 \le T_f < 20^oC \\ 996.9 \times \left(1 - 3.17 \times 10^{-4}\right)\left(T_f - 25\right) - 2.56 \times 10^{-6}\left(T_f - 25\right)^2\right) & 25 \le T_f < 250^oC \\ 1758.4 + 10^{-3}T_f\left(-4.8434 \times 10^{-5} + T_f\left(1.0907 \times 10^{-5} - 9.8467 \times 10^{-9}T_f\right)\right) & 250 \le T_f < 300^oC \end{cases} \tag{2}$$

$$\mu_f = \begin{cases} 10^{-3} \times \left(1 + 0.015512\left(T_f - 20\right)\right) & 0 \le T_f < 100^oC \\ 0.2414 \times 10^{-3} \times 10^{\left(\frac{247.8}{T_f + 133.15}\right)} & 100 \le T_f < 300^oC \end{cases} \tag{3}$$

$$C_f = 12010.1 - 80.4T_f + 0.3T_f^2 - 5.4 \times 10^{-4}T_f^3 + 3.6 \times 10^{-7}T \quad 273.1K \le T_f < 573.15K \tag{4}$$

$$\lambda_f = -0.8691 + 0.0089T_f - 1.5837 \times 10^{-5}T_f^2 + 7.9754 \times 10^{-9}T \quad 273.1K \le T_f < 573.15K \tag{5}$$

where ρ_w is the working fluid density, kg/m^3; λ_w is the thermal conductivity of working fluid, W/(m·K); cw is the specific heat capacity of working fluid, J/(kg·K); T_f is the temperature of working fluid, ^oC; and μ_w is the dynamic viscosity of the working fluid, Pa·s.

2.2. Governing equations

2.2.1. Mass conservation equation in the EGS

In the discrete fracture network DFN, fluid flow is formulated based on the following mass conservation equation [13,20]:

$$\frac{\partial\left(\rho_w\varphi_f\right)}{\partial t} + \nabla \cdot \left(\rho_w u_f\right) = -Q_f \tag{6}$$

where φ_f is the porosity of the fracture; t is the time, s; Q_f is the resource term of the fracture, kg/(m^3·s); and u_f is the velocity of the working fluid in the DFN, m/s, which is given by the following equation [13,20]:

$$u_f = -\frac{k_f}{\mu_w}(\nabla p) \tag{7}$$

where k_f is the fracture permeability, m^2; p is the pore pressure in the fracture, Pa.

2.2.2. Energy balance equation in the EGS

Overall, the HDR matrix is almost impermeable. Considering this, the energy balance equation can be expressed by Refs. [13,20]:

$$\rho_r c_r \frac{\partial T_r}{\partial t} - \nabla \cdot \left(\lambda_r \nabla T_r\right) = Q_{fE} \tag{8}$$

where ρ_r, T_r, c_r, and λ_r re the density (kg/m^3), temperature (^oC), specific heat capacity (J/(kg•^oC)), and thermal conductivity (W/(m·K)) of the HDR matrix, respectively, and Q_{fE} is the corresponding heat resource (W/m^3).

Convective heat transfer dominates within the DFN. Assuming local thermal equilibrium between the fluid and rock matrix, the fluid temperature is taken to be equal to the rock temperature. The corresponding energy conservation equation is given as follows [13,20]:

$$\rho_w c_w \frac{\partial T_f}{\partial t} + \rho_w c_w u_f \cdot \nabla T - \nabla \cdot \left(\lambda_w \nabla T\right) = -Q_{fE} \tag{9}$$

In the equation above, ρ_w is the fluid density, kg/m^3; T_f is the temperature in the fracture,°C; c_w is the heat capacity of the working fluid, J/(kg·K); λ_w is the thermal conductivity of the fluid, W/(m·K).

2.2.3. Mass conservation equation in the CCGS

To improve computational efficiency when considering the CCGS, the wellbore is simplified as a 1D line element. Considering this setting, the mass conservation equation in the outer pipe can be expressed by the following equations [8,14,25]:

$$\frac{\partial(A_{c1}\rho_w)}{\partial t}+\nabla\cdot\left(A_{c1}\rho_w u_{f,p1}\right)=0 \tag{10}$$

$$\rho_f\frac{\partial u_{f,p1}}{\partial t}=-\nabla p_1-\frac{1}{2}f_D\frac{\rho_f}{d_p}|u_{f,p1}|u_{f,p1} \tag{11}$$

$$f_D=8\left[\left(\frac{8}{\mathrm{Re}}\right)+\left(k_a+k_b\right)^{-1.5}\right]^{1/12} \tag{12}$$

$$k_a=\left[-2.457\ln\left(\left(\frac{7}{\mathrm{Re}}\right)^{0.9}+0.27\left(\frac{e}{d_p}\right)\right)\right]^{1.6} \tag{13}$$

$$k_b=\left(\frac{37530}{\mathrm{Re}}\right)^{16} \tag{14}$$

where A_{c1}, $u_{f,p1}$,p_1,f_D, d_p and Re denote the outer pipe cross-sectional area (m^2), velocity (m/s), pressure (Pa), Darcy friction factor, pipe diameter (m), roughness (m), and Reynolds number, respectively.

The mass conservation equation in the inner pipe can be expressed by the following equations [8,14,25]:

$$\frac{\partial(A_{c2}\rho_w)}{\partial t}+\nabla\cdot\left(A_{c2}\rho_w u_{f,p2}\right)=0 \tag{15}$$

$$\rho_f\frac{\partial u_{f,p2}}{\partial t}=-\nabla p_1-\frac{1}{2}f_D\frac{\rho_f}{d_p}|u_{f,p2}|u_{f,p2} \tag{16}$$

where A_{c2} denotes the borehole cross-sectional area of the outer pipe (m^2), $u_{f,p2}$ is the velocity in the outer pipe (m/s); p_2 is the pressure in outer pipe (Pa);

2.2.4. Energy balance equation in the CCGS

In this study, the energy conservation equation in the one-dimensional inner pipeline is represented by Refs. [8,14,25]:

$$\rho_f A_{c1}c_w\frac{\partial T_{f1}}{\partial t}+\rho_f A_{c1}c_2u_{f,p1}\cdot\nabla T_{f,p1}-\nabla\cdot\left(A_c\lambda_w\nabla T_{f1}\right)=\frac{1}{2}f_D\frac{\rho_f A_{c1}}{d_p}|u_{f,p1}|u_{f,p1}^2-Q_1 \tag{17}$$

$$Q_1=2\pi r_0(hZ)_{eff}\left(T_{f1}-T_{f2}\right) \tag{18}$$

In the above equations, $T_{f,p2}$ is the temperature in the annulus, °C; T_{f1} is the fluid temperature in the inner pipe, °C; and Q_1 represents the source term of the energy balance equation, W/m^3. The detailed spatial distribution of the pipe well is presented in Fig. 2.

$$h=\frac{Nu\cdot\lambda_f}{d_p} \tag{19}$$

where Nu denotes the Nusselt number, which characterizes the convective heat transfer between the working fluid and the pipe wall. It is calculated using the Gnielinski correlation [26], as follows:

$$Nu=\frac{(f_D/8)\cdot(\mathrm{Re}-1000)\cdot\mathrm{Pr}}{1+12.7\sqrt{f_D/8}\left(\mathrm{Pr}^{2/3}-1\right)} \tag{20}$$

where P_r is the Prandtl number. Considering the thermal behavior within the outer pipe, the heat transfer process is characterized [8,14,25]:

$$\rho_f A_{c2}c_f\frac{\partial T_{f2}}{\partial t}+\rho_f A_{c2}c_f u_{f,p2}\cdot\nabla T_{f2}-\nabla\cdot\left(A_{c2}\lambda_f\nabla T_{f2}\right)=\frac{1}{2}f_D\frac{\rho_f A_c}{d_p}|u_{f,p2}|u_{f,p2}^2+Q_2—Q_1 \tag{21}$$

$$Q_2=2\pi r_0(hZ)_{eff}\left(T_r-T_{f2}\right) \tag{22}$$

where T_{f2} is the temperature of fluid in the inner pipe, °C; Q_2 is the external heat exchanged through the casing wall, W/m^3.

2.3. Definitions of the characteristic parameters

In the EGS system, the production temperature of the horizontal well can be calculated by:

$$T_{out}=\frac{\int_L T(t)dl}{L} \tag{23}$$

where L is the length of the horizontal well, m; $T(t)$ is the temperature of the horizontal well at different time instants, °C. Also, the output power of the EGS system is calculated by:

$$P_E=qc_w(T_{out}-T_{in}) \tag{24}$$

where P_E is the output power of the EGS system, MW, where q is the flow rate of the circulating fluid, kg/s.

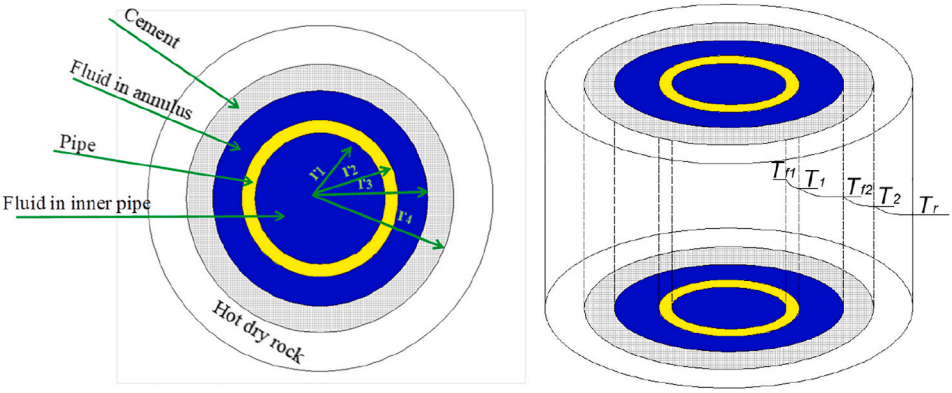


Fig. 2. Spatial distribution of temperature along the pipe well.

Table 1
Parameters used for model validation.

Parameters	Value
T_{in} (injection temperature)	30°C
T_0 (initial temperature)	150°C
V_{in} (injection velocity)	0.001 m/s
λ_r (matrix thermal conductivity)	3 W/(m·K)
ρ_r (matrix density)	3000 kg/m^3
ρ_w (water density)	1000 kg/m^3
C_r (matrix heat capacity)	1000 J/(kg·K)
C_w (water heat capacity)	4000 J/(kg·K)
D_f (fracture aperture)	0.001 m

2.4. Model validation

2.4.1. Model validation of the thermal-hydraulic coupling model of EGS

Model validation is conducted by comparing the present results with the analytical and numerical solutions of Lauwerier [27,28], which describe temperature evolution in a single fracture. A two-dimensional single-fracture configuration is adopted, where the initial fracture temperature is 150°C. A fluid at 20°C is injected at a constant velocity of 0.01 m/s from one boundary, extracting heat from the surrounding rock matrix. The resulting temperature field is obtained using following equations, with the required parameters provided in Table 1.

$$T_r(x,z,t) = T_0 + (Tin - T_0)erfc\left(\frac{2\lambda_r + |z|\rho_f C_{p,f} V_{in} b_F}{2\rho_f C_{p,f} V_{in} b_F}\sqrt{\frac{\rho_f C_{p,f} V_{in}}{\lambda_r (V_{in} + x)}}\right) \quad (25)$$

$$T_f(x,z,t) = T_0 + (T_{in} - T_0)erfc\left(\frac{\lambda_x}{2\rho_f C_{p,f} V_{in} b_F}\sqrt{\frac{\rho_f C_{p,f} V_{in}}{\lambda_r (V_{in} + x)}}\right) \quad (26)$$

Model validation is illustrated in Fig. 3 through comparison between numerical and analytical results. The close correspondence between the two sets of results verifies the robustness and predictive capability of the proposed numerical framework.

2.4.2. Model validation of CCGS model

Validation of the numerical model was performed using experimental data from the literature [28]. The experiment involved a test well of 1800 m depth, with an inner pipe length of 1780 m (110 mm × 10 mm), constructed from an insulated plastic tube, and operated at a flow rate of 40 m^3/h. Model parameters were calibrated using the experimental heat transfer data. The simulated outlet temperatures closely match the measured values, confirming the accuracy and predictive capability of the model (Fig. 4(a)). The reliability of the prediction model was further assessed through error analysis. The overall Mean-Absolute Percentage Error (MAPE) is 3.18%, indicating a low average prediction deviation (Fig. 4 (b)). This error characteristic of converging over time, combined with the deviation of less than 4% in most periods, confirms that the model can reliably reflect the long-term behavior of the system and meet the requirements of engineering applications.

2.4.3. Model Validation of EGS-CCGS model

In this study, a triaxial stress experiment was designed to investigate the coupled geothermal extraction performance of an Enhanced Geothermal System (EGS) and a Closed Coaxial Geothermal System (CCGS). The experimental setup (Fig. 5), and the detailed parameters are listed in Table 2. The test specimen consisted of a 200 × 200 × 200 mm fractured granite core, which was then encased in concrete to form a 300 × 300 × 300 mm cube. The concrete served primarily as a sealing layer to prevent fluid leakage to the exterior of the specimen, ensuring that heat transfer occurred predominantly within the granite. Boreholes were drilled through the specimen to connect the fracture network, forming the EGS system, and an additional borehole was drilled above the fracture to install the CCGS system. The specimen was then placed inside a triaxial stress chamber and subjected to stresses of 25 MPa, 20 MPa, and 25 MPa along the three principal directions. Heating plates integrated into the triaxial chamber raised the specimen temperature to 100°C. Subsequently, water at 25°C was injected into the EGS at a rate of 20 mL/min, while the CCGS was supplied at a rate of 2 mL/min. The outlet temperatures of both the EGS and CCGS were continuously monitored. A corresponding numerical simulation model was also developed, and the simulated outlet temperatures of the EGS and CCGS were compared with the experimental measurements, as shown in Fig. 6. The close agreement between simulation and experimental results confirms the high reliability of the proposed model.

3. Combined EGS-CCGS system

3.1. Model description

Fig. 7 presents the conceptual modeling framework for the combined EGS-CCGS system. The geometric model domain is represented by a simplified cubic reservoir of 500 m^3, located at a depth of 4 km. The development process begins with the drilling of horizontal injection and production wells for the EGS from the surface to the target geothermal formation, with hydraulic fracturing employed to establish connectivity between them (Fig. 7(a)). Following this, the CCGS horizontal well is drilled, after which cementing operations are performed, and casing is installed to ensure wellbore integrity and stability. Finally, the insulated inner pipe is inserted to form the coaxial well configuration, as illustrated in Fig. 7(b). The CCGS consists of a 4350-m vertical well with a 2000-m horizontal section, with adjacent wells spaced at 100 m intervals. This spacing provides a balance between limiting thermal interference and reducing drilling [16]. In the EGS, circulating fluid extracts heat from connected fractures via the injection well.

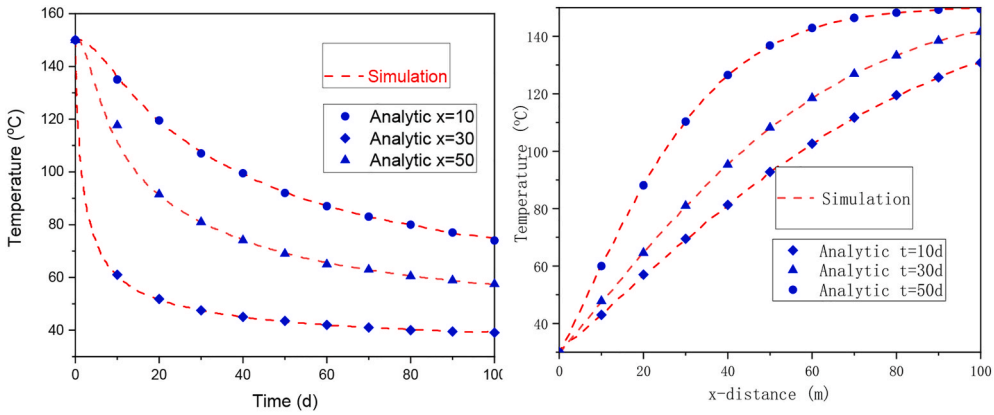


Fig. 3. Model Validation of Thermal-Hydraulic coupling model of EGS (d: day).

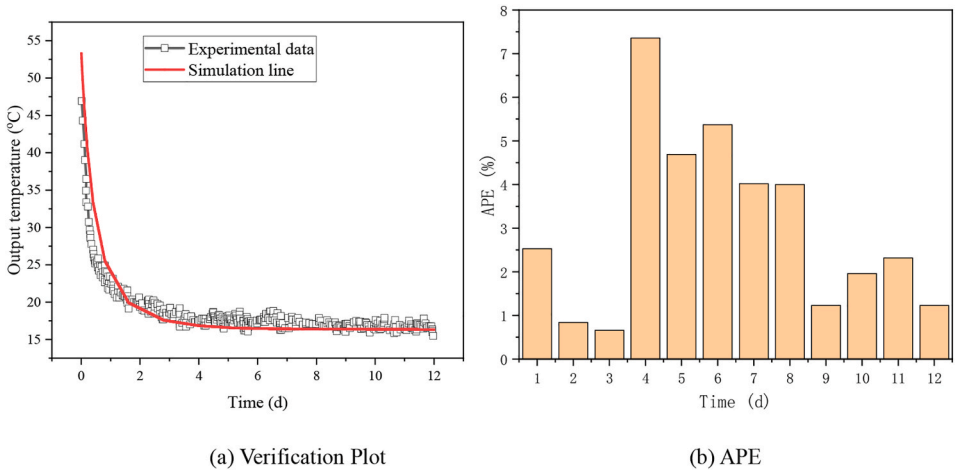


Fig. 4. Model Validation of CCGS model (d: day).

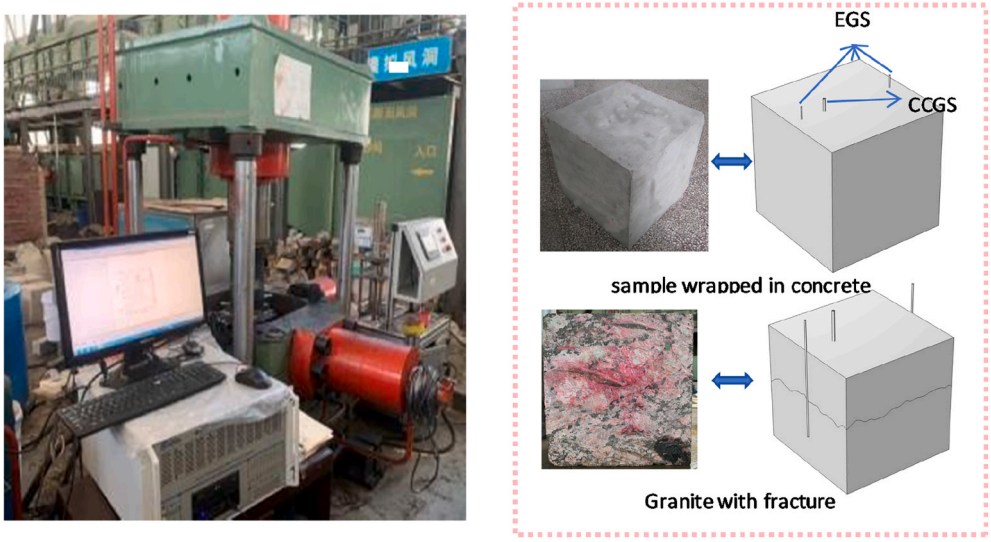


Fig. 5. Schematic diagram of the experimental design.

Table 2
Parameters used for model validation of EGS-CCGS.

Parameters	Value
Sample size	200 × 200 × 200 mm
EGS injection pipe size	φ 3 mm
Inner pipe size of CCGS	φ 3 mm
outer pipe size of CCGS	φ 5 mm
Injection rate of EGS	20 ml/min
Injection rate of CCGS	2 ml/min
Injection temperature	25°C
ρ_w (water density)	1000 kg/m^3
C_r (matrix heat capacity)	1000 J/(kg·K)
C_w (water heat capacity)	4000 J/(kg·K)
D_f (fracture aperture)	0.001 m

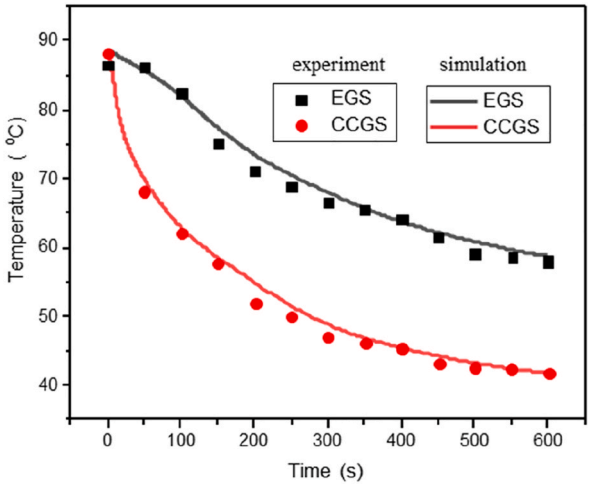
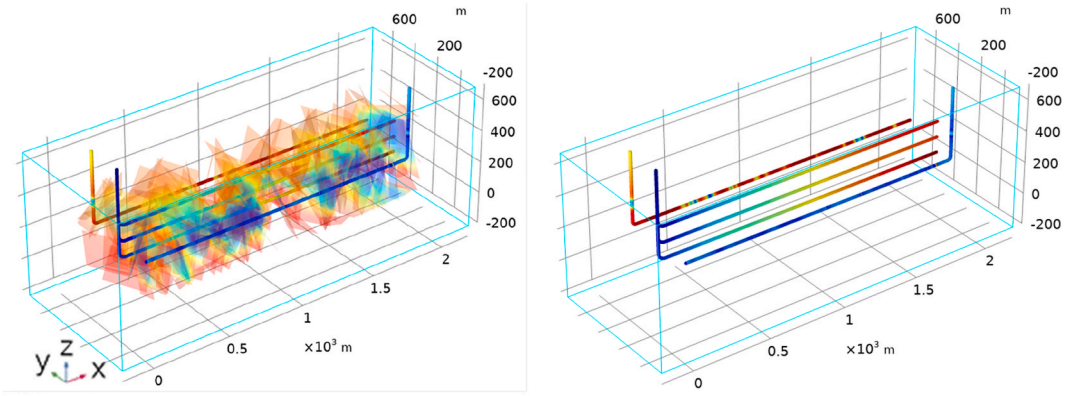


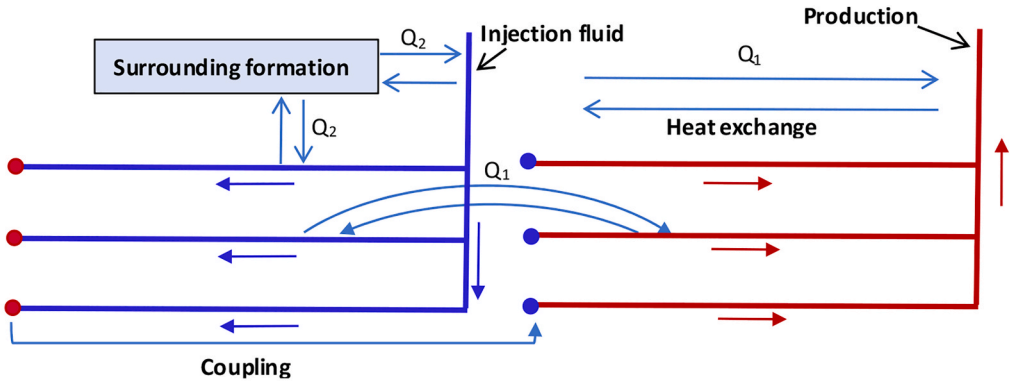
Fig. 6. Validation of the EGS-CCGS model.

Concurrently, the CCGS injects low-temperature fluid into the coaxial annulus, where it absorbs heat from the rock matrix and exits through the inner pipe.

The convective heat transfer process within coaxial wells can be described using one-dimensional line elements, as illustrated in Fig. 7 (c), which allows for integrating the temperature, pressure, and flow rate coupling terms. When injecting into the outer pipe, the pipe absorbs heat from the reservoir (Q_2-Q_1) to heat the well fluid. The flow velocity



(a) Combined EGS-CCGS geothermal system (b) EGS with CCGS wellbore layout



(c) Schematic diagram of the one-dimensional CCGS system

Fig. 7. Geometric modeling of the proposed combined system.

at the bottom of the outer pipe is taken as the injection flow velocity of the inner pipe, and the pressure of the inner pipe is set equal to the outlet pressure of the outer pipe. The temperature at the bottom of the outer tube is used as the injection temperature for the inner pipe. Concurrently, a process of heat exchange (Q_1) occurs between the internal and external tube fluids.

The stochastic DFN is generated based on statistical distributions of fracture geometric parameters rather than randomly assigning fracture properties without constraints. The fracture length (L) and dip angle (θ) are treated as stochastic variables following prescribed probability distributions within the defined parameter ranges [29]. The spatial orientation of each fracture is described in the global coordinate system using the azimuth and inclination angles, which characterize its horizontal orientation and deviation from the vertical direction, respectively.

For illustrative purposes, a case study involving 300 fractures is presented to demonstrate the generation of a discrete fracture network. The fracture diameters were categorized into four ranges: 100 m, 200 m, 300 m, and 400 m, aligned with the Weibull distribution. In the spherical coordinate system, azimuth and inclination angles adhere to a normal distribution, as shown in Fig. 8(a–c). The fracture distribution probability function is employed to determine the number of fractures corresponding to different diameter classes, dip angles, and azimuth orientations (Fig. 9(a–c)).

3.2. Initial and boundary conditions and parameters

A geothermal gradient of 0.044°C/m is used to determine the initial reservoir temperature, as given by:

$$T = T_0 + \nabla T \cdot Z \tag{27}$$

where T_0 is the ground surface temperature (°C), Z represents the distance from the surface to the reservoir (m), and ∇T is the geothermal gradient, which is set at 0.044°C/m. Additionally, the heat transfer from the surrounding boundaries to the interior of the model takes place under the following boundary conditions:

$$n \cdot q = h(T_{ext} - T) \tag{28}$$

The injection temperature is set to 20°C in both EGS and CCGS, while the production well in the EGS system is treated as a free boundary. The initial pressure field is established according to a hydrostatic pressure gradient of 9.81 MPa/km. By specifying a pressure of 39.2 MPa at the top reservoir boundary, the reservoir pressure distribution is obtained using:

$$p = 39.2 + \nabla p \cdot Z \tag{29}$$

The injection flow rate is set to 80 kg/s for the EGS and 20 kg/s for the CCGS. The outlet pressure of each system is set equal to the reservoir pressure at its respective location.

3.3. Mesh and model solution

Meshing of the combined EGS–CCGS system model was conducted using COMSOL Multiphysics. The reservoir matrix was discretized into a three-dimensional tetrahedral mesh (Fig. 10(a)), with mesh refinement applied in the stimulated reservoir region to improve resolution (Fig. 10 (b)). The discrete fracture network was represented by a two-dimensional surface mesh (Fig. 10(c)), while the geothermal wells were modeled using a one-dimensional line-element mesh (Fig. 10(d)). This simplification aims to capture the overall heat exchange behavior of the coaxial well at the reservoir scale rather than the local flow

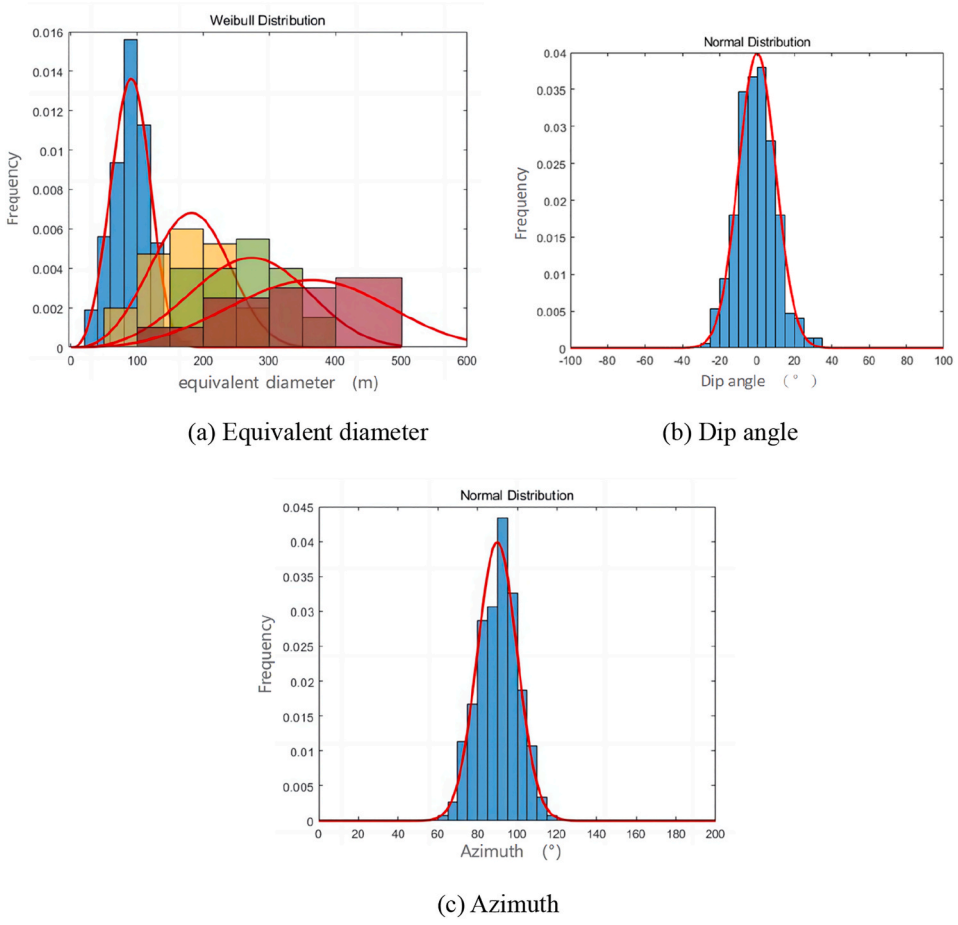


Fig. 8. Probability distribution of the (a) equivalent diameter, (b) dip angle, and (c) azimuth of fractures.

structures inside the annulus. The final mesh consisted of 2,425,072 tetrahedral elements. The integration of 3D, 2D, and 1D meshes enabled a substantial reduction in computational time. Key simulation parameters are summarized in Tables 3 and 4. Nonlinear problem solving employed adaptive time stepping, with Jacobian matrix updates activated to address strong thermo-hydraulic coupling effects.

4. Results and discussion

4.1. Analysis of the flow and temperature fields

Fig. 11 shows the evolution of seepage and temperature fields in a HDR reservoir with coaxial wells. The first row of subfigures highlights the velocity field; the red streamline represents the area with faster flow velocity and better fracture connectivity, thereby delineating the dominant seepage channels within the fractured reservoir. In highly connected fracture zones, the local flow velocity reaches as high as 8.3 $\times 10^{-6}$ m/s, while in poorly connected areas, the flow velocity decreases to 0.1 $\times 10^{-6}$ m/s. These channels indicate the fluid flow mainly along the connected fractures from the injection well to the production well. As the heat extraction, it is found that the red line streamline increases gradually, indicating that the flow of the connecting fractures is better. The reason for the increase in streamline is due to the increase in permeability of fractures after they contract with cold water.

The second row of subfigures depicts the temporal evolution of reservoir pressure. The results shown in the figure highlight the formation of a high-pressure zone near the injection well. It can be seen from the figure that the pressure difference is 3.4 MPa, and the fluid resistance is 0.034 MPa/(kg·s). This indicates that the fluid resistance is lower than the requirement for hot dry rock development, which specifies that fluid resistance must be less than 0.1 MPa/(kg·s). With continued heat extraction, the pore pressure of the reservoir gradually decreases. This reduction in high-pressure zones is attributed to the enhancement of reservoir permeability as the formation temperature declines, which in turn lowers fluid resistance and results in a corresponding decrease in reservoir pressure.

In addition, the third row of subfigures shows the variations in the reservoir temperature field over time. Initially, temperature reduction is concentrated around the EGS injection well and the CCGS wellbore. As the heat extraction process goes on, the low-temperature area of the EGS system exhibits an expansion towards the production well along the connected fractures, while the low-temperature region associated with the CCGS system spreads radially throughout the reservoir. The simulation results show that the low-temperature area of the reservoir almost covers the entire reservoir after 50 years. Notably, even in zones with limited fracture connectivity, there is a significant decrease in temperature due to the heat absorption of coaxial wells. These findings demonstrate that both systems are working to enhance the heat transfer process, jointly promoting the efficient development of the reservoir over a period of approximately 50 years.

Finally, the fourth row of subfigures illustrates the variations in the temperature of the CCGS system coaxial well over time. Initially, the inlet temperature is at 20°C, while the bottom hole temperature reaches approximately 125°C. With the progression in the injection process, the bottom hole temperature is found to exhibit a gradual decrease until stabilizing at a temperature around 60°C. This sustained elevation of the internal fluid temperature within the CCGS well confirms the system's capacity for effective heat extraction, thereby demonstrating the technical feasibility of CCGS-based geothermal heating.

Furthermore, to better characterize and explain the pattern of

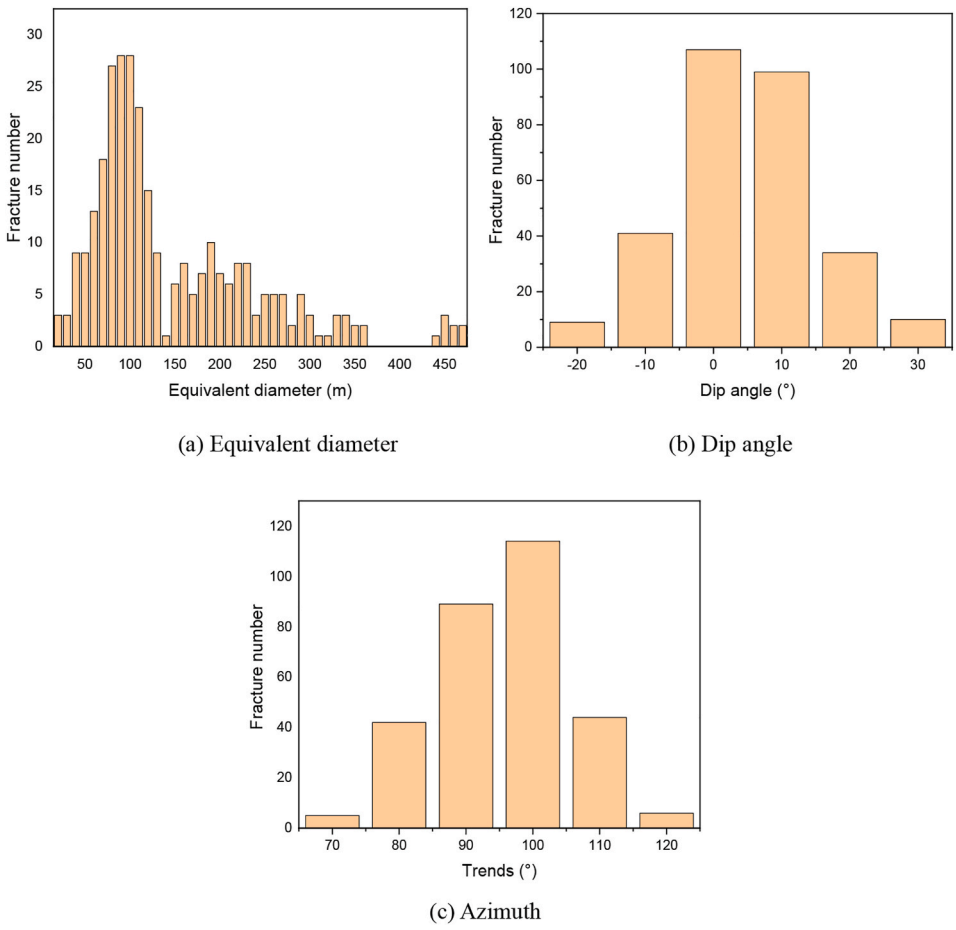


Fig. 9. Distribution of the number of fractures at different (a) equivalent diameter, (b) dip angle, and (c) azimuth of fractures.

reservoir temperature variation, observation lines ab and cd, and observation planes Z = 250 and Y = 250 are defined and set in the model, as presented in Fig. 12. On this basis, Fig. 13(a) shows the variation in the reservoir temperature over the observation line ab with the progression in the production time. Initially, the low-temperature areas are found to be located around the fractures, while the temperature of the rock matrix around the fractures is relatively high. With the progression in the heat extraction time, the temperature of the rock matrix around the fracture exhibits a gradual decrease. After 50 years, the temperature of the rock matrix around the fracture decreases to as low as 60°C. It is worth noting here that the drop in the temperature of the rock matrix around the fracture is no longer obvious at 60 years, indicating that thermal depletion in the fracture vicinity approaches a steady state.

In addition, the variation in the reservoir temperature over the observation line cd is shown in Fig. 13(b). It is noted here that the position of $x = 200$ m is the position of the EGS injection well, $x = 700$ m is the position of the EGS extraction well, and $x = 450$ m is the position of the CCGS coaxial well. The results reveal that the low-temperature fluid injected at the EGS well gradually gains heat during its migration toward the production well. At this stage, the outlet temperature of the production well reaches approximately 210°C, while the reservoir temperature has dropped at the coaxial well location. These changes in temperature confirm that the CCGS system effectively enhances the heat extraction efficiency of HDR reservoirs. Moreover, at the coaxial well location, the rock mass temperature is 100°C, indicating that heat from the surrounding rock is being absorbed by the CCGS system. Notably, the relatively high production temperature in the EGS system demonstrates that heat uptake by the CCGS does not impair EGS operational performance. As the heat extraction time progresses, the temperature at the production well location is found to drop to 90°C at 50 years, beyond which the rate of decline becomes negligible, suggesting that thermal depletion approaches a quasi-steady state after 60 years.

The EGS system exhibits a higher production temperature in the initial stages of operation, with this elevated level sustained over a longer duration, as shown in Fig. 14. On the other hand, the outlet temperature of the CCGS system can be maintained at a level above 100°C in the first 10 years and above 90°C in the first 20 years. These results demonstrate the strong potential of the CCGS system to operate as an effective complement to the EGS system, thereby enhancing the overall thermal recovery performance of HDR reservoirs.

4.2. *Comparisons of the combined system against the standard EGS*

This section presents a comparative analysis of the heating performance of the combined EGS-CCGS system versus a conventional EGS. Fig. 15 presents the temperature field distribution characteristics of the combined and traditional systems at cross-sections Z = 250 and Y = 250 at 30 years of operation. First, the temperature field characteristics are compared at the Z = 250 section. In the combined EGS-CCGS system, the temperature of the reservoir around the Z = 250 fracture is not much different. However, the combined system has a 2000-m-long absorption belt around the coaxial well. This belt allows for enhancing the reservoir heating efficiency. At the cross-section Y = 250, as shown in Fig. 15(c) and (d), the variations in the temperature field of the two systems considered are more obvious. At 30a, it is shown that the low-temperature zone of the reservoir around the fractures in the EGS system occupies a relatively small proportion of the entire cross-section. In contrast, the three coaxial casing wellbores in the combined system extract heat directly from the rock matrix adjacent to non-connected

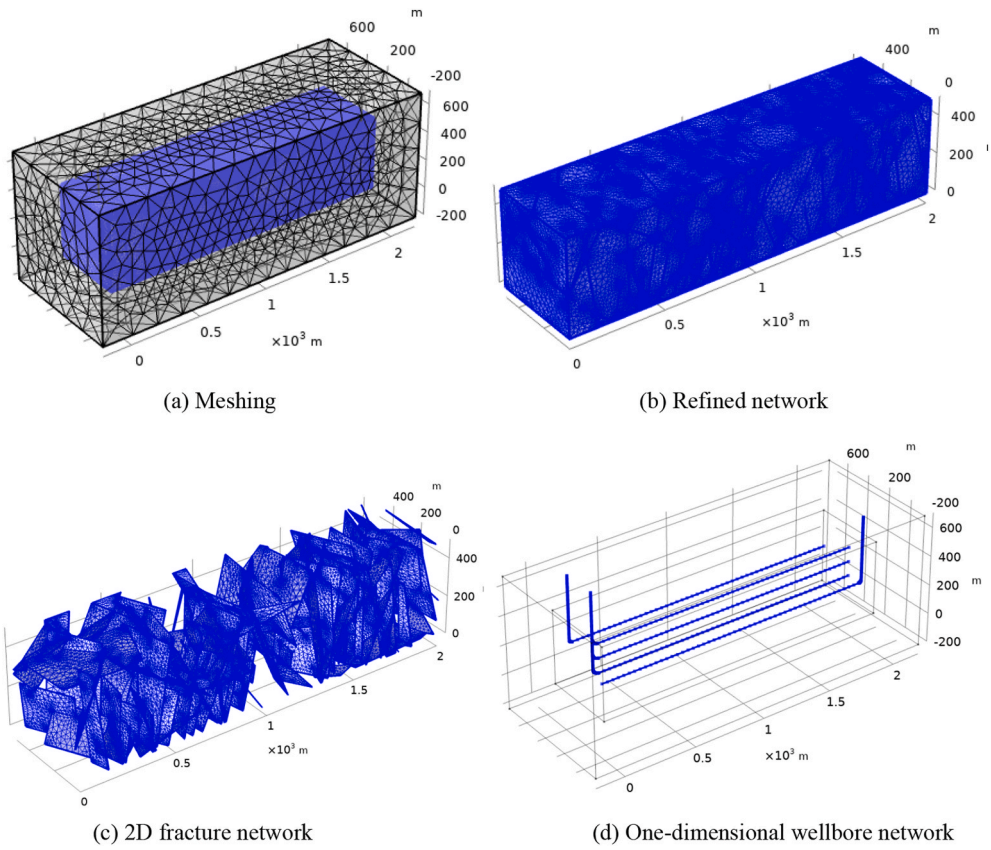


Fig. 10. Meshing details.

Table 3
Parameters used in the numerical simulation of the combined EGS system [27, 30–32].

Component	Density (kg/m^3)	Porosity	Permeability (m^2)	Thermal conductivity (W/(m.K))	Specific heat capacity (J/(kg·K))
Rock matrix	2800	0.05	10^{-18}	2.8	800
Fracture	1200	1	Eq. (1)	1	1200

Table 4
Parameters used in the numerical simulation of the combined CCGS system [27, 30–32].

items	Value (m)	items	Value (W/(m•K))
Inner radius of inner pipe	0.0506	Thermal conductivity of casing	43.75
Outer radius of inner pipe	0.0889	Thermal conductivity of cement	0.93
Inner radius of casing	0.1594	Thermal conductivity of inner pipe	0.025
Inner radius of horizontal well	0.2159		

fractures, resulting in a markedly larger proportion of low-temperature zones. Overall, the findings demonstrate that the combined EGS-CCGS system significantly increases the heat extraction efficiency in the non-connected fracture area as compared to the traditional EGS system.

Fig. 16 compares the temporal evolution of heat generation between the combined EGS–CCGS system and the conventional EGS system. Initially, the combined system yields 80 MW, which decreases to 32 MW after 60 years, whereas traditional EGS starts at 65 MW and drops to 25 MW over the same period. Additionally, to compare the enhancement in the heat generation efficiency of the combined EGS-CCGS system compared to the EGS system, the power growth coefficient is defined, as presented in Eq. (30). The results show that during early-stage mining, the growth coefficient can exceed 20%, signifying that the integration of the CCGS system enhances mining efficiency by more than one-fifth. As production continues, the growth coefficient line decreases to around 12% before increasing again after that. This trend is attributed to the sustained heat absorption from the reservoir by the CCGS system, which progressively increases its contribution to total power generation.

$$\eta = \frac{P_{ESG+CCGS} - P_{EGS}}{P_{EGS}} \tag{30}$$

4.3. Parametric analysis

4.3.1. Injection rate

This section investigates the heat extraction performance of the combined EGS-CCGS system under varying injection rates. Production power is compared across EGS injection rates of 40, 60, 80, 100, and 120 kg/s, paired with CCGS injection rates of 10, 15, 20, 25, and 30 kg/s.

Fig. 17 presents the variation of the production power of the combined EGS–CCGS system with the progression in the extraction time for different combinations of EGS and CCGS injection rates. As shown in the figure, at a constant CCGS injection rate, as the EGS injection rate increases, increasing the EGS injection rate leads to a steady rise in the production power, indicating a positive correlation between EGS flow rate and system output. The variation of production power over time can be divided into two stages. From 0 to 30 years, production power increases gradually with injection rate. But after the injection rate increased to 120 kg/s, the growth rate of thermal power slowed down. In

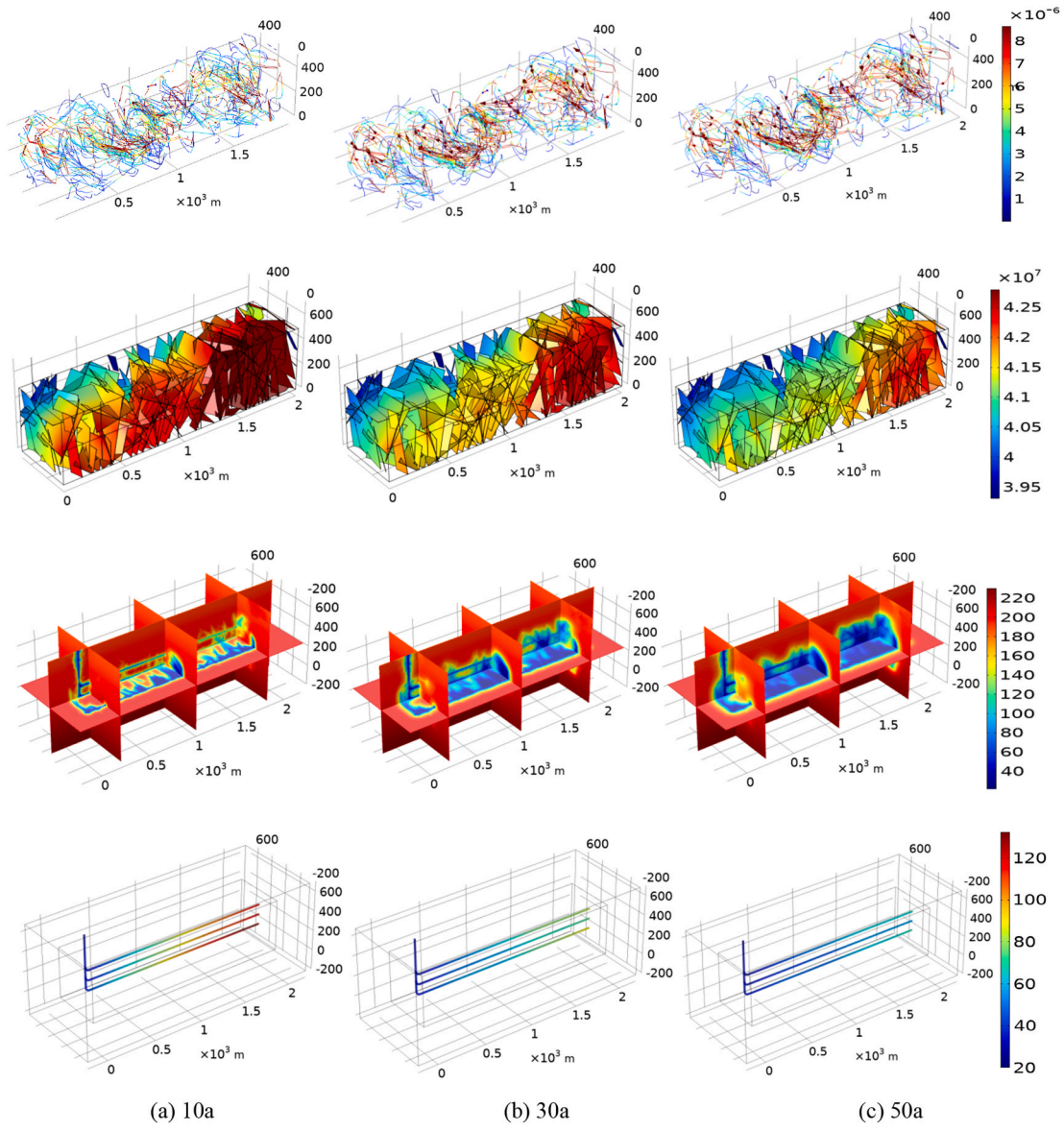


Fig. 11. The evolution of the velocity (first row), pressure (second row), and temperature (third row) contours in the reservoir over time, as well as the temperature in the coaxial closed loop well (fourth row), under an injection rate of EGS of 80 kg/s and a rate of CCGS of 20 kg/s.

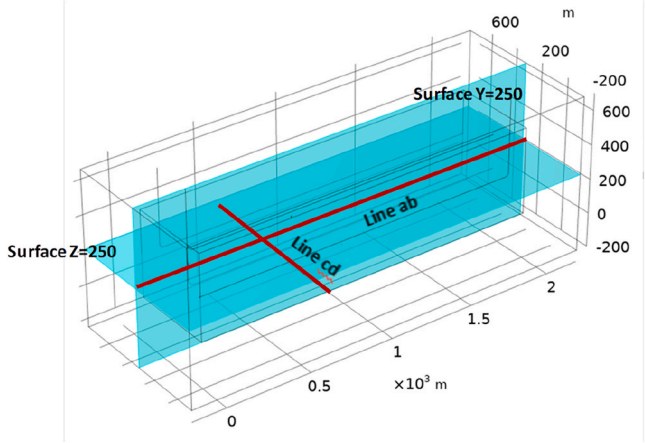


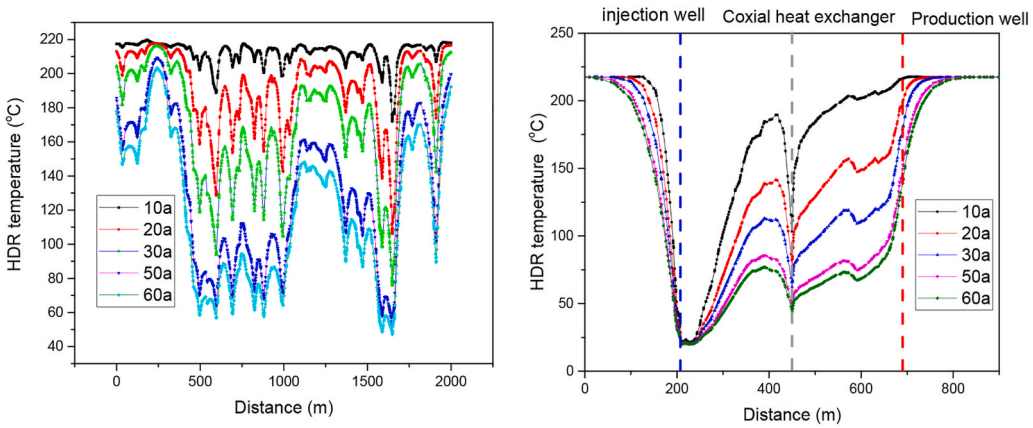
Fig. 12. Schematic diagram of the observation surface and observation line.

the second stage of 30-60 years, the rate of increase in thermal power with increasing injection rate is limited, especially after the injection rate reaches 120 kg/s, the thermal power hardly increases significantly in 30-60 years. Based on these findings, a fluid injection rate of 120 kg/s is utilized for the EGS production system.

In the subsequent analysis, the EGS injection rate is fixed at 120 kg/s to examine how production power varies over time under different CCGS injection rates. As shown in Fig. 18, increasing the injection rate of the CCGS system leads to progressive rise in the production power of the combined EGS-CCGS system, which approaches a plateau at approximately 30 kg/s. Based on these results, a CCGS injection rate of 25 kg/s is identified as the optimal injection rate.

4.3.2. *Number of hydraulic fractures*

To investigate the effect of fracture number on the heat transfer performance of the combined EGS-CCGS system, numerical models with 100, 200, 300, and 400 fractures were developed. For each configuration, the heat extraction performance of the combined system was analyzed considering different fracture numbers, an EGS injection rate of 120 kg/s, and a CCGS injection rate of 25 kg/s.



(a) Line ab (b) Line cd

Fig. 13. Temperature distribution along lines ab and cd over time.

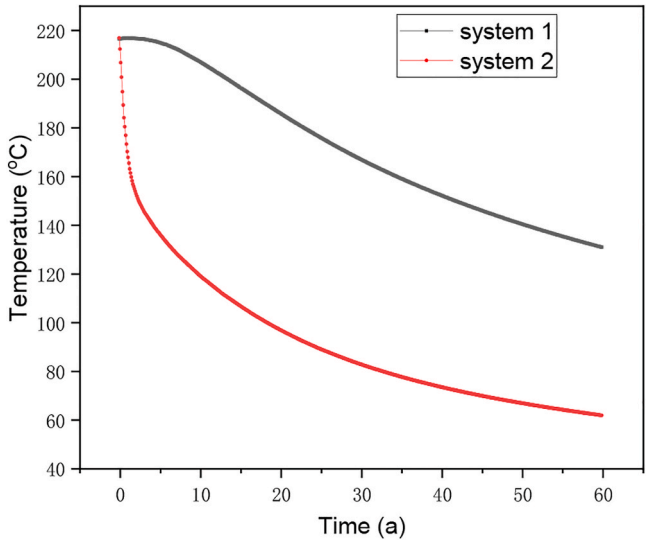


Fig. 14. The variation in outlet temperatures of the EGS system (red) and the CCGS system (black) with time.

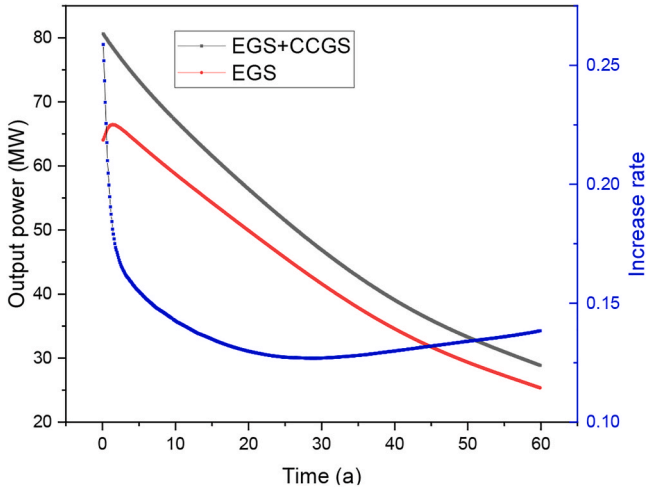
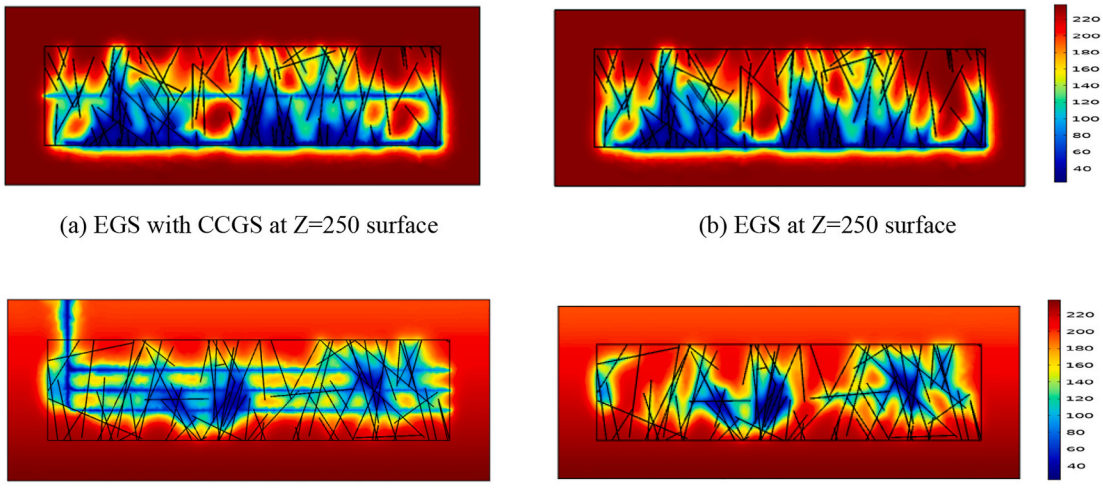


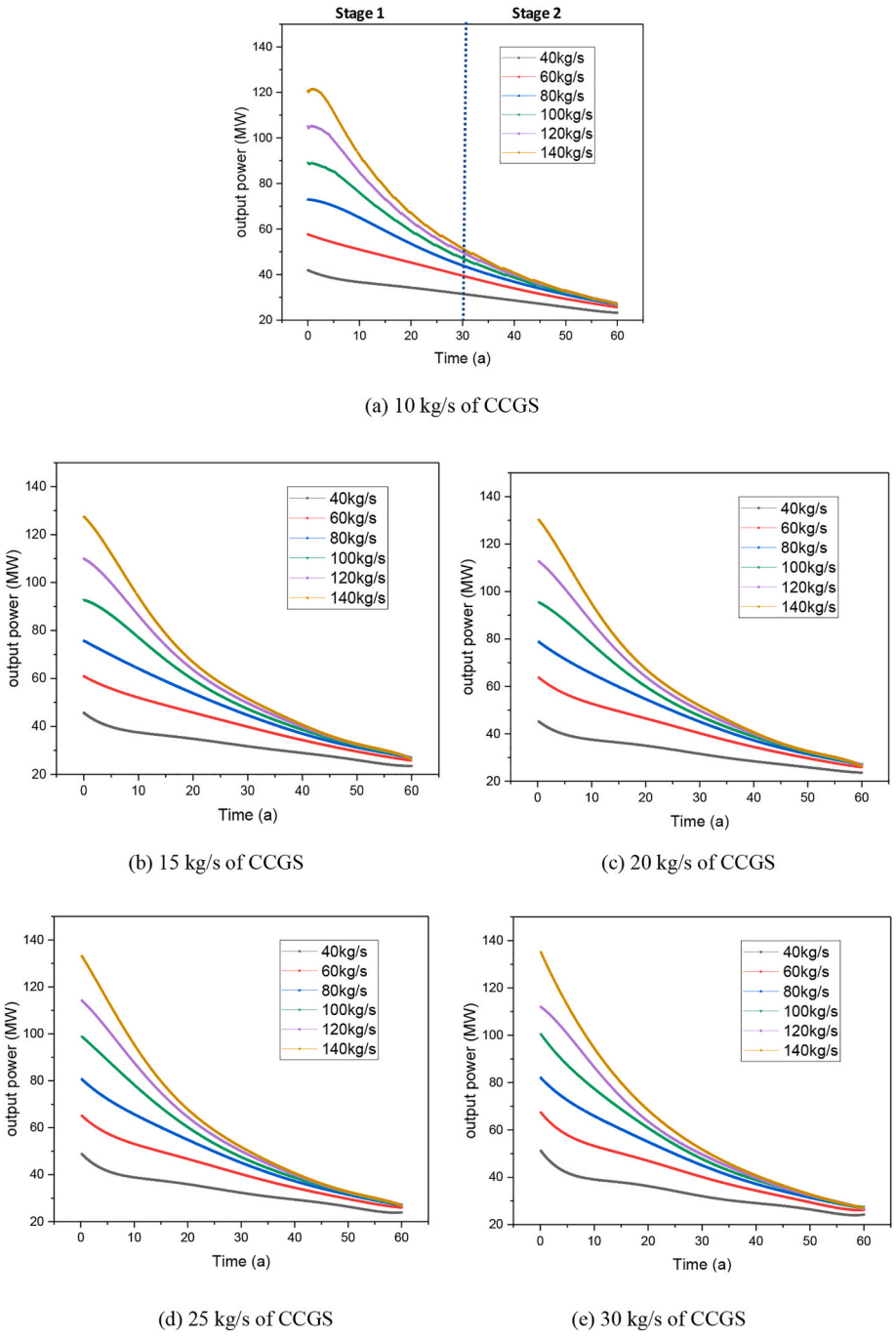
Fig. 16. Comparison of the heating power of the combined EGS-CCGS system and the traditional EGS system, with a fracture number of 300.



(a) EGS with CCGS at Z=250 surface (b) EGS at Z=250 surface

(c) EGS with CCGS at Y=250 surface (d) EGS at Y=250 surface

Fig. 15. The temperature field distribution characteristics of the combined and traditional EGS systems at the cross-sections Z = 250 and Y = 250 at 30 years, with a rate of EGS of 80 kg/s and a rate of CCGS of 20 kg/s.



(a) 10 kg/s of CCGS

(b) 15 kg/s of CCGS

(c) 20 kg/s of CCGS

(d) 25 kg/s of CCGS

(e) 30 kg/s of CCGS

Fig. 17. Variation of the production power with the extraction time under different injection rates of CCGS and EGS combinations.

Fig. 19 shows the temperature contour at the cross-section Y = 250 for the combined system mining after 30 years of operation under different fracture numbers. With 100 fractures, the proportion of low-temperature zones around the fractures is relatively small, with only two fracture areas exhibiting significant cooling; most of the low-temperature regions are concentrated around the CCGS wellbore, underscoring the critical role of the CCGS system in HDR reservoir exploitation under poor fracture connectivity. With 200 fractures, additional low-temperature areas appear around the fractures, although the CCGS wellbore still accounts for a large share of the cooled areas. With 300 fractures, the connected area of the fractures exhibits a significant increase. Also, the proportion of the low-temperature areas around the fractures significantly increases, while the proportion of low-temperature areas around the CCGS wellbore decreases. In contrast, with 400 fractures, it is noted that the low-temperature zones are mainly concentrated in the central region of the reservoir, with peripheral areas retaining relatively high temperatures. This can be explained by the fact that numerous fractures create dominant flow channels, resulting in the formation of fluid short circuits. Overall, in cases with 100 and 200 fractures, the proportion of the low-temperature areas around the CCGS system is relatively larger than in the other two cases, indicating that the CCGS system plays a dominant role.

Since different fracture models were generated using stochastic functions, the random generation process inherently affects fracture connectivity. For each fracture-number scenario, 100 stochastic DFN realizations were produced. At each time step, the ensemble mean and sample standard deviation were calculated, and the 95% confidence interval of the mean was determined to construct the corresponding

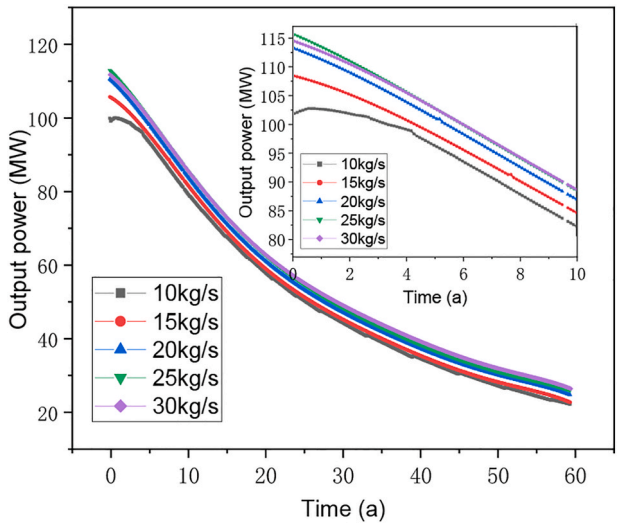


Fig. 18. Effect of the injection rate on the heating power of the CCGS system at an EGS injection rate of 120 kg/s.

sensitivity bands. Fig. 20 depicts the variation in production power over time as a function of fracture density within EGS and CCGS reservoirs. For systems containing 100 to 300 fractures, production power exhibits a positive correlation with fracture number. This increase is attributed to the expanded heat exchange surface area between the working fluid and the hot dry rock (HDR) matrix, thereby enhancing thermal transfer efficiency. The greater fracture density provides increased flow paths and contact area, enabling the working fluid to absorb more thermal energy from the reservoir, consequently elevating output power.

However, when the fracture number reaches 400, production power declines significantly. This reduction results from excessive fracture interconnectivity, which facilitates premature thermal breakthrough. As illustrated in Fig. 19(d), this condition leads to fluid short-circuiting, whereby the working fluid traverses the reservoir too rapidly to allow adequate heat extraction from the surrounding rock. Consequently, the system's thermal recovery efficiency diminishes. This phenomenon of declining efficiency at high fracture densities due to short-circuiting is consistent with observations reported in the literature [16].

Across different fracture numbers, the sensitivity bandwidth exhibits a clear decreasing trend. When the fracture number is relatively low (≈100), the sensitivity band is widest, indicating that stochastic variations in fracture geometry have the greatest impact on flow paths and heat transfer efficiency, leading to pronounced power fluctuations. As the fracture number increases to a moderate level (≈200), the band narrows significantly, reflecting enhanced connectivity and a more stable system response. At higher fracture numbers (≈300 and above), the sensitivity band becomes even narrower and approaches stability, suggesting that thermal recovery is predominantly governed by connected fractures, with minimal influence from stochastic variability. However, at extremely high fracture numbers, local fluid short-circuiting may cause a slight rebound in uncertainty over specific time intervals. Furthermore, the sensitivity bandwidth tends to expand during the early production stage and contract over time, with variability peaking initially before stabilizing in the long term.

Fig. 21 shows the temporal variation of the CCGS heat extraction increase rate for different fracture numbers. At a fracture number of 100, the initial recovery increase rate is approximately 40%, increasing to 150% after 60 years. This indicates that the CCGS makes a substantial contribution to heat extraction in the later stages of operation. When the number of fractures increases to 200, the initial increase rate is 20%, and it subsequently climbs to 80%. However, when the number of fractures reaches 300, the increase rate decreases markedly to around 20%. For 400 fractures, only a minor increase in the recovery rate is observed. This slight increase is attributed to the fluid short - circuit, which reduces the heat extraction efficiency of the EGS system, while the

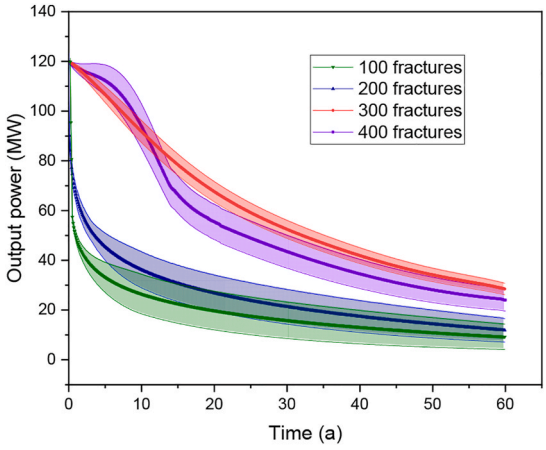


Fig. 20. Variation in the output power with the progression in the heat extraction time under different fracture numbers. (a: year).

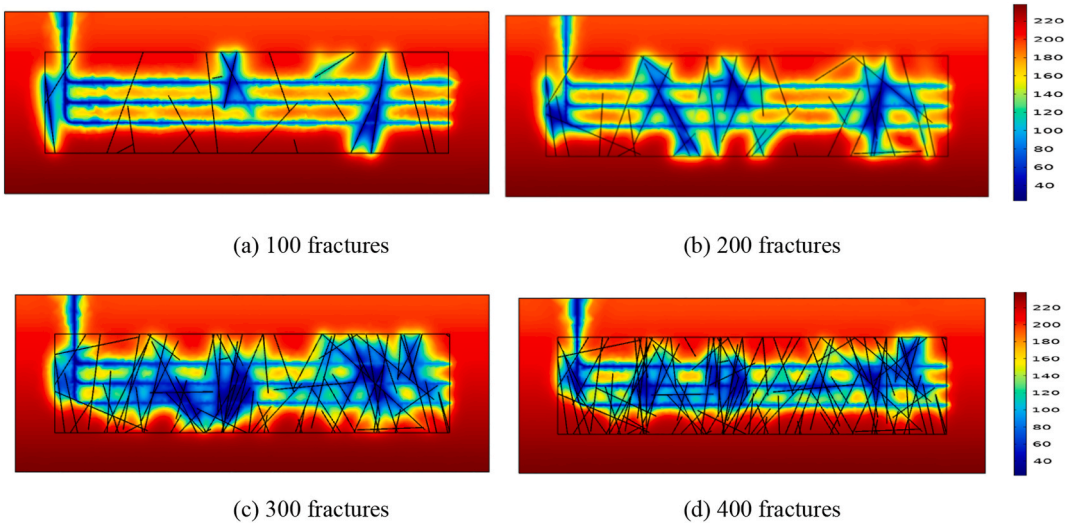


Fig. 19. Temperature contours under different fracture numbers after 30 years, considering an EGS rate of 120 kg/s and a CCGS rate of 25 kg/s.

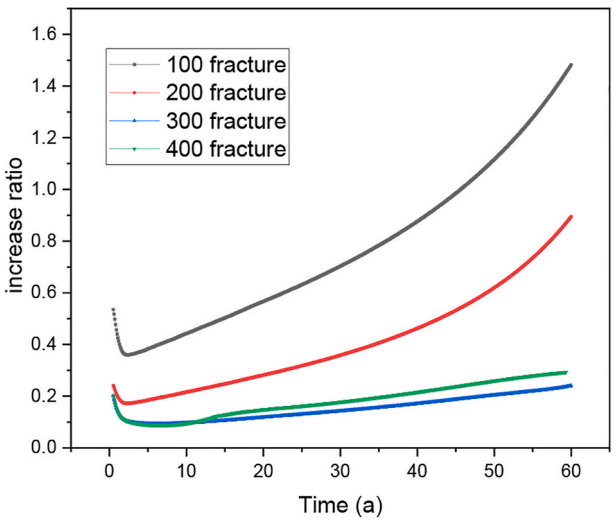


Fig. 21. The enhancement rate of the CCGS system heat extraction under different fracture numbers.

contribution rate of the CCGS system relatively increases.

As the number of fractures increases, the contribution of CCGS gradually decreases. This is because more fractures usually improve the connectivity of the fracture network, allowing the EGS circulating fluid to enter a larger heat transfer area through the connected fractures and obtain more heat from the reservoir matrix. On the contrary, when the number of fractures is small, the lack of fracture connectivity limits the fluid circulation and reduces the heat extraction capacity of EGS. At this time, CCGS can directly obtain the heat in the high-temperature rock mass near the low-connected fracture through the wellbore heat transfer method, thereby increasing its contribution ratio. However, the increase in the number of cracks will not infinitely improve the performance of EGS. When the fracture connectivity is too high, a dominant flow channel may be formed, which shortens the fluid residence time, reduces the heat exchange efficiency, and increases the risk of thermal breakthrough. Therefore, fracture connectivity needs to be balanced between fluid circulation capacity and sufficient heat transfer time. By providing additional heat extraction paths, CCGS reduces the dependence of the system on the highly connected fracture network and improves the heat utilization efficiency of the reservoir matrix.

In addition, it should be pointed out that in this paper, the number of fractures is used as a control parameter to construct fracture network scenarios with different fracture development degrees, rather than directly defining it as a quantitative index of fracture connectivity. The actual fracture network connectivity is also affected by the geometric characteristics of fractures [33], including fracture direction, dip angle, strike, length distribution and fracture crossover probability. Therefore, the increase of fracture number mainly reflects the change of extent of fracture network development, and its influence on fluid migration path and heat exchange efficiency is still related to the specific fracture structure characteristics.

4.3.3. Thermal conductivity of Hot dry rock

To assess the impact of uncertainties in thermal conductivity (λ) and permeability (k) on system production forecasts, this study generated n = 100 discrete fracture network (DFN) realizations for each thermal conductivity and permeability scenario under a fixed fracture number, and performed full-period numerical simulations for each case. The ensemble mean of the 100 DFN simulation results was then calculated to obtain the temporal variation of output power, as shown in Fig. 22. Due to differences in fracture connectivity, output power exhibits fluctuations. Although fracture randomness influences the output power, the mean values display a stable temporal trend, indicating the reliability of the predictions.

Fig. 22 further shows the effect of the variation in thermal conductivity on the heat production power, revealing distinct trends dependent on fracture density. With 100 fractures, heat transfer efficiency peaks when conductivity increases to 2.8 W/(m·K), where power rises from 7975 kW to 9549 kW representing a 19.7% growth rate. When the thermal conductivity coefficient continues to increase, the growth rate of production power slows down. For instance, when the thermal conductivity coefficient rises from 5.6 W/(m·K) to 7.0 W/(m·K), the production power increases by 4.5%. For 200 fractures, the growth rate of production power decreases with increasing thermal conductivity, with conductivity increase from 1.2 W/(m·K) to 2.8 W/(m·K) producing merely 10.9% growth (11,124 kW to 12,335 kW) and from 5.6 W/(m·K) to 7.0 W/(m·K) yielding minimal 1.15% growth (13,167 kW to 13,318 kW). With 300 fractures, the influence of thermal conductivity coefficient on the thermal efficiency of the combined EGS-CCGS system becomes limited. When fracture connectivity is poor due to a small fracture count, the CCGS system contributes a relatively large share of the total heat extraction. Since the CCGS primarily depends on thermal conduction through the rock matrix to deliver heat to the coaxial well, increasing thermal conductivity inevitably enhances its heat extraction efficiency, thereby boosting the overall system performance. However, as the number of fractures increases, the role of thermal conductivity in improving heat extraction diminishes sharply.

4.3.4. Fracture permeability

This study demonstrates that while the thermal conductivity coefficient exerts a significant influence on heat transfer efficiency when fracture numbers are relatively low, increasing fracture permeability under such conditions has minimal impact. As presented in Fig. 23, quantitative analysis reveals that under a fracture density of 100 fractures, increasing permeability from 1-fold to 5-fold elevates power generation from 9549 GWh to 10,906 GWh, yielding an absolute increase of 1357 GWh and a total growth of 14.21%, while exhibiting progressively diminishing returns with only 1.97% growth rate during the 4-fold to 5-fold permeability stage. For the 200-fracture configuration, equivalent permeability enhancement boosts power generation from 12,335 GWh to 16,690 GWh, representing an absolute increment of 4355 GWh and a total increase of 35.28%. When fracture density reaches 300 fractures, the 1-fold to 5-fold permeability augmentation drives power generation from 30,148 GWh to 38,219 GWh, achieving an absolute rise of 8071 GWh and a total enhancement of 26.79%.

This indicates that permeability enhancement has a relatively limited impact on total power output when the fracture count is 100. This is because when the fracture connectivity is poor, the energy generated by the CCGS system accounts for most of the energy generated by the geothermal system. Additionally, it is noted here that the variation in fracture permeability mainly affects the EGS system. Thus, in the combined EGS-CCGS system, the permeability variation has almost no effect in cases where there are fewer fractures. On the other hand, with a larger number of fractures, the connectivity of the fractures is significantly enhanced. In this case, the heat generation capacity of the EGS system dominates. At the same time, the permeability of the fractures increases, leading to an increase in heat generation efficiency. The more cracks there are, the greater the impact of fracture permeability on the thermal recovery efficiency of the system. This is because the increase in fracture permeability mainly enhances the ability of fractures to transport working fluids. Therefore, increasing the number of fractures while increasing fracture permeability will significantly improve the system's heat extraction efficiency.

The increase in permeability continuously enhances production capacity throughout the entire production cycle. Moreover, under high-permeability conditions, the sensitivity band is narrower, indicating that fluid flow is less affected by variations in the stochastic fracture network. In contrast, under low-permeability conditions, the sensitivity band is wider, reflecting that, under flow-restricted conditions,

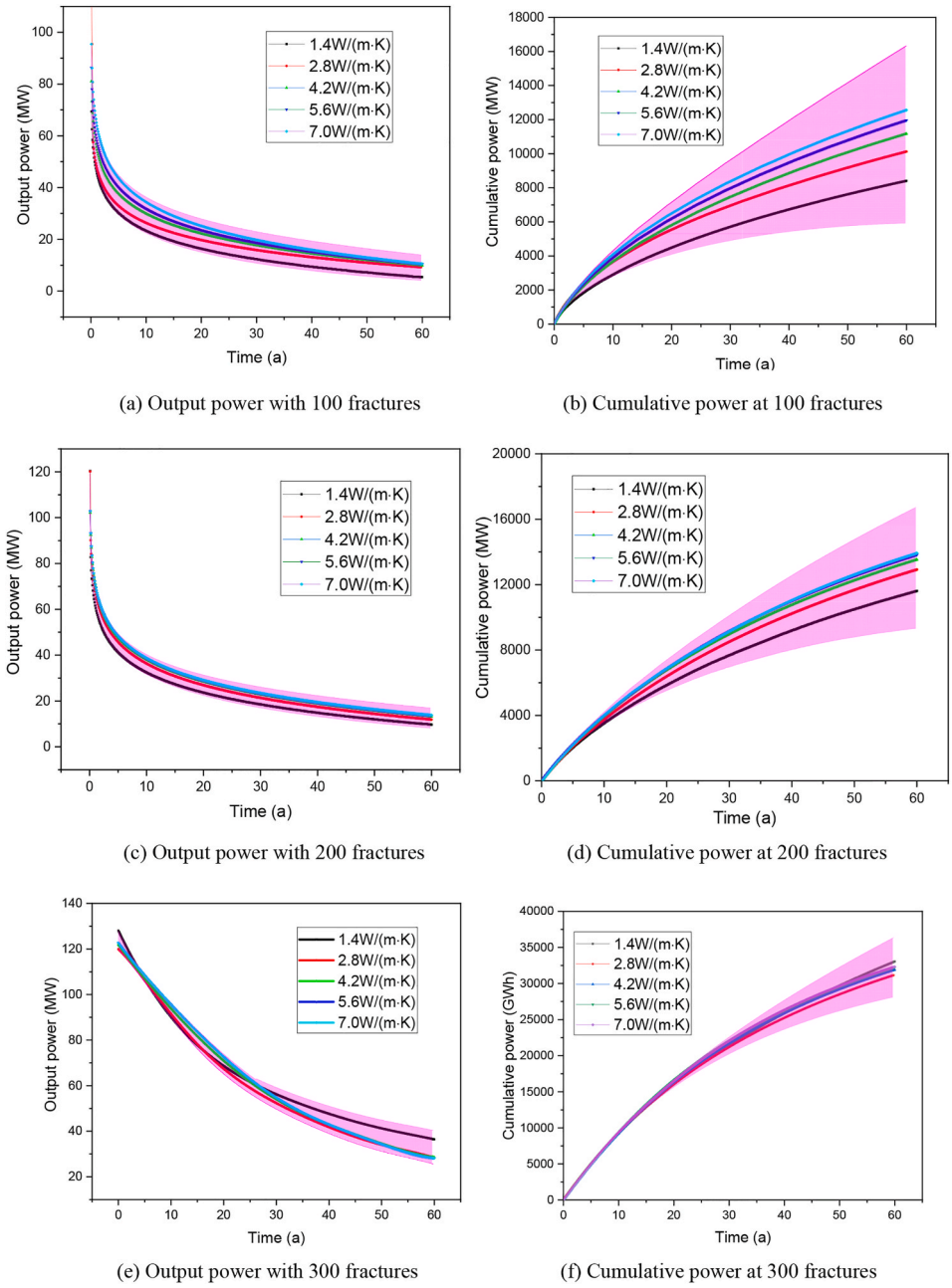


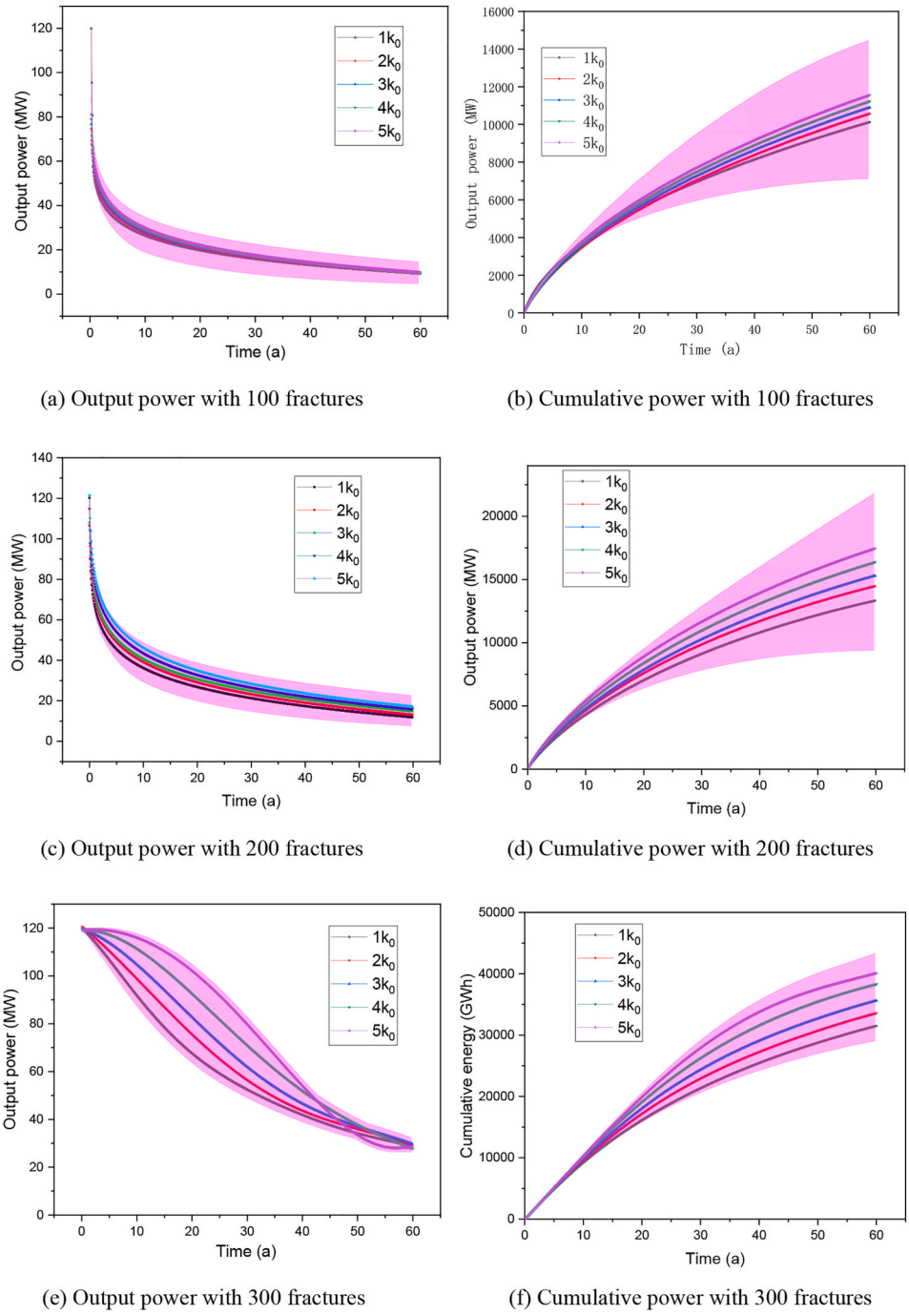
Fig. 22. The effect of thermal conductivity on the heat production power under different fracture numbers.

production capacity is highly sensitive to fracture connectivity.

4.3.5. *Sensitivity analysis*

From Fig. 24(a), cumulative power increases rapidly at first and then more slowly with the rise of injection rate, while with increasing CCGS injection rate, it first increases and then decreases. Therefore, the injection rates need to be jointly optimized. For example, the combination of EGS at 120 kg/s and CCGS at 25 kg/s can achieve the peak production capacity (29,744 kWh), whereas excessive injection (e.g., CCGS at 30 kg/s) results in efficiency reduction. From Fig. 24 (b), fracture count has a significant effect on cumulative power. When the number of fractures increases from 100 to 400, the changes in cumulative power are 92.7%, 97.5%, and −10.3%, respectively. This indicates that variations in fracture number substantially influence cumulative power, and power output is highly sensitive to fracture count. From Fig. 24 (c), the influence of thermal conductivity on power varies with fracture number. When the fracture count is 100, increasing thermal conductivity from 1.2 to 7 leads to cumulative power increases of 22.1%, 10.6%, 7.4%, and 4.8%, respectively. When the fracture count is 200, the corresponding increases are 10.9%, 10.6%, 7.4%, and 4.8%. However, when the fracture count is 300, changes in thermal conductivity result in negligible variations in cumulative power. This shows that poorer fracture connectivity makes cumulative power more sensitive to thermal conductivity. Cumulative power increases linearly with permeability across different fracture numbers, and the growth rate is higher when the fracture number is greater in Fig. 24 (d).

To evaluate the relative influence of each parameter on the cumulative power output, the contribution ratios of different factors were calculated as shown in Fig. 25. Fracture number, permeability, EGS injection rate, CCGS injection rate, and thermal conductivity account for 54.7%, 26.6%, 12.1%, 3.4%, and 3.2% of the total impact, respectively. This demonstrates that cumulative power output is most sensitive to



(a) Output power with 100 fractures (b) Cumulative power with 100 fractures

(c) Output power with 200 fractures (d) Cumulative power with 200 fractures

(e) Output power with 300 fractures (f) Cumulative power with 300 fractures

Fig. 23. The effects of the fracture permeability on the heat production power (k_0 is the initial permeability).

fracture number, followed by fracture permeability, while its sensitivity to injection rate and thermal conductivity is comparatively lower.

5. Discussion

5.1. Economic analysis

The costs associated with geothermal energy development primarily include resource exploration, power plant construction, well drilling, operation, and maintenance. In this study, a simplified levelized cost of electricity (LCOE) is calculated as the ratio of the total life-cycle cost to the cumulative electricity generation, following the approach adopted in previous economic assessments of EGS projects. Although conventional LCOE calculations generally account for the time value of money through a discount rate, discounting is not considered here. This simplified formulation is adopted to ensure methodological consistency with previous studies and to facilitate a direct comparison among the system configurations investigated. The calculation method for the surface cost is given by the following equation [32]:

$$C_{surf} = 4.5 + \frac{2000 \times P_t}{10^6} \tag{31}$$

where C_{surf} denotes the surface cost (M$), and P_t is the power generation (kWh).

Regarding the drilling costs estimation, a predictive model was derived from field data, as summarized in Table 5. For the vertical well

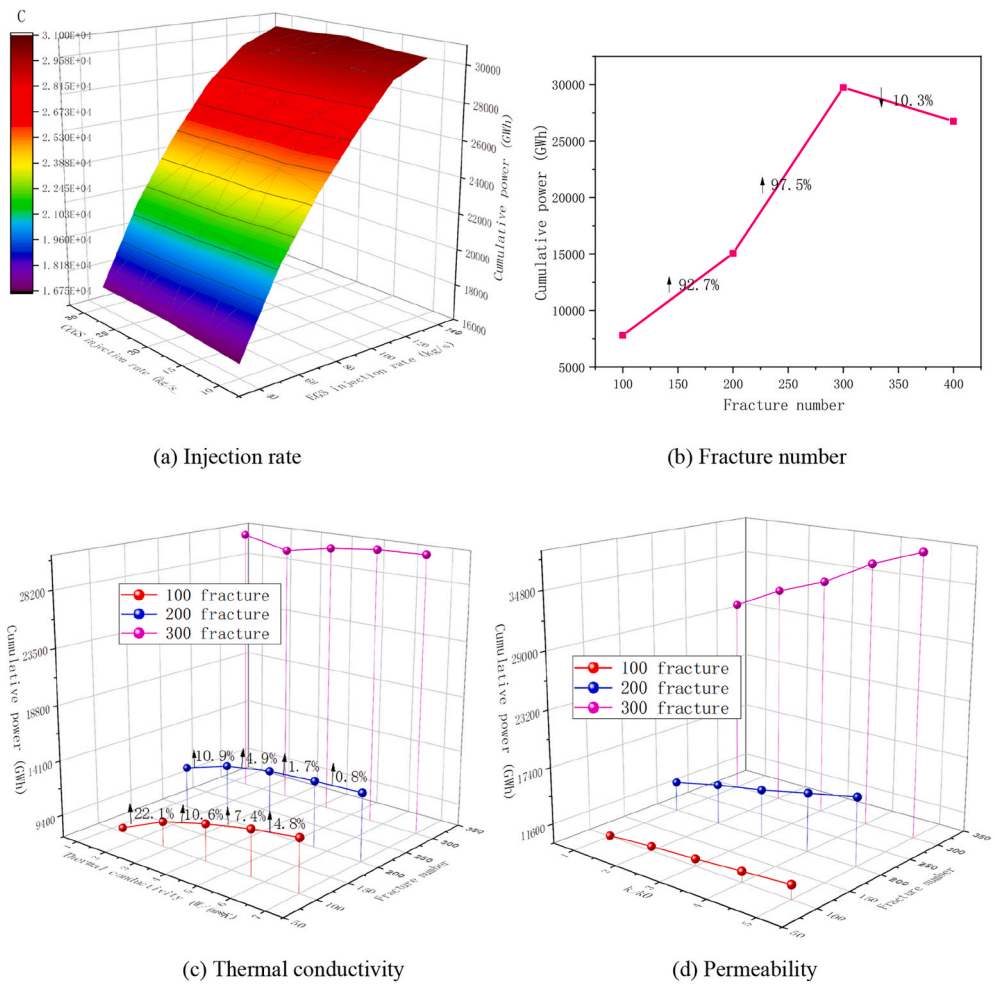


Fig. 24. Parameter sensitivity analysis.

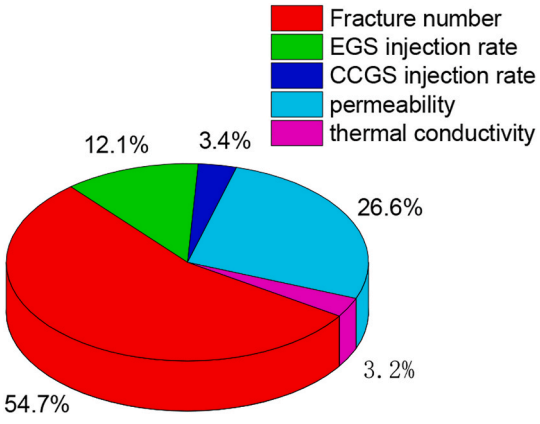


Fig. 25. Analysis of parameter impact proportion.

depth of 4500 m, the drilling cost is $2.75 million USD. The calculation based on Lukawski's dataset yields a value of USD 5.84 million; however, considering the dataset's temporal limitations, this estimate was adjusted by a factor of 0.5 in accordance with recent technological advancements and updated references, resulting in a revised cost of USD 2.87 million. In contrast, the cost prediction derived from Bloomfield et al. produces negative values, rendering it unsuitable for deep-well drilling cost assessment. Comparative analysis indicates that the results of Lei's predictive model and the adjusted Lukawski model are broadly consistent. As Lei's model is based on an empirical formula derived from the average drilling costs of vertical and horizontal wells in contemporary geothermal drilling projects, it was selected as the basis for drilling cost estimation in this study [34].

Table 5
Drilling cost model.

References	Data sources	Formula
Lei et al., 2020 [34]	Drilling cost data in China (Geothermal well)	$C_{well} = (600H_v + 1500H_h) \times 10^{-6}$
Lukawsiki et al., 2014 [35]	1976–2009 API JAS data (Oil and gas well)	$C_{well} = 1.65 \times 10^{-5}H^{1.607}$
Lukawsiki et al., 2016 [35]	1976–2009 API JAS data (geothermal well)	$C_{well} = 1.172 \times 10^{-7}H^2 + 2.3 \times 10^{-3}H - 0.62$
Bloomfield et al., 2005 [36]	Drilling costs data from 1997 to 2000 for Central America and the Azores	$C_{well} = 1.194 \times 10^{-12}H^3 - 3.86510^{-8}H^2 - 6.399 \times 10^{-4}H - 0.007$

Where C_{well} is the drilling cost, M$; H_v is the vertical well length, m; H_h is the horizontal well length, m; H is the well length, m.

The unit cost (CO&M) of the O&M costs is calculated using Equation (32) in this study. Additionally, the following equation can be used to estimate the operation cost [34]:

$$C_{ope} = 0.02C_{well} + 20\exp[-0.0025(P_t - 5)] \quad (32)$$

where C_{ope8} denotes the operation cost (M$), and C_{well} is the drilling cost (M$). Using the different costs presented above, the levelized cost of energy (*LCOE*), ($/kWh), can be calculated as follows:

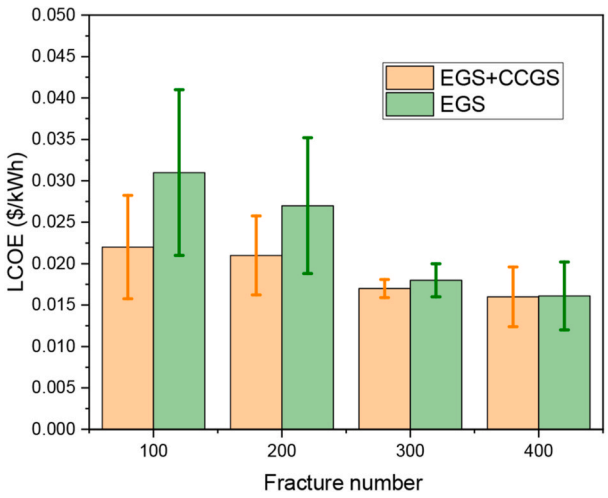


Fig. 26. Comparison of the LCOE of the combined EGS-CCGS system and the traditional EGS system.

$$LCOE = \frac{C_{surface} + C_{well} + C_{ope} + C_{fracture}}{P_t} \tag{33}$$

Due to the stochastic nature of fracture generation, the calculated LCOE exhibits certain fluctuations under different fracture numbers, as shown in Fig. 26. The results show that for fracture numbers of 100, 200, 300, and 400, the LCOEs of the EGS-CCGS system are 0.022, 0.021, 0.017, and 0.016 $/kWh, respectively. Under the same conditions, the corresponding LCOEs of the conventional EGS system are 0.031, 0.027, 0.018, and 0.016 $/kWh, which are 29%, 20%, 5%, and 0.6% higher than those of the EGS-CCGS system, respectively. Error analysis indicates that the fluctuation amplitude of LCOE for both systems decreases with increasing fracture number, and the relative error of the EGS system is significantly higher than that of the EGS-CCGS system at lower fracture numbers. This suggests that fewer fractures lead to greater uncertainty in prediction results, while at higher fracture numbers, the error differences between the two systems tend to converge.

Furthermore, Fig. 27 presents the impact of thermal conductivity on the LCOE under different fracture numbers, along with the associated uncertainties. For 100 fractures, increasing the thermal conductivity from 1.4 to 5.6 W/m·K reduces the LCOE from 0.0239 to 0.0215 $/kWh, while the uncertainty narrows from ±0.0083 to ±0.0065. A similar trend is observed for 200 fractures, where the LCOE decreases from 0.0220 to 0.0205 $/kWh, and the uncertainty is reduced from ±0.0063 to ±0.0048. These results suggest that higher thermal conductivity improves the economic performance and leads to more stable predictions. In addition, the relative error is consistently lower in the 200-fracture case than in the 100-fracture case, indicating a stabilizing effect of increasing fracture number.

For 100 fractures, the LCOE decreases from 0.0232 to 0.0214 $/kWh as permeability increases, while the uncertainty narrows from ±0.0062 to ±0.0047. However, the reduction is relatively small due to the overlap in the error ranges. When the fracture number increases to 300, the effect of permeability becomes more evident: the LCOE decreases from 0.0172 to 0.0158 $/kWh, with uncertainty further reduced from ±0.0011 to ±0.0009. The narrower uncertainty range at higher fracture density suggests a more stable system response, indicating that permeability plays a more consistent role in reducing LCOE.

5.2. Comparison of different geothermal systems

Fig. 28 compares the LCOE of EGS, CCGS, and EGS–CCGS systems based on the data in Table 6. For EGS, the LCOE varies from 0.0341 to 0.047 $/kWh, with the lowest value obtained for the multi-vertical-well configuration using the DFN model. In horizontal well systems, the triple-horizontal-well configuration with a dual-porosity model shows a 21.3% lower LCOE than the parallel fracture model, underscoring the sensitivity of economic performance to fracture modeling.

Conventional single-well CCGS systems exhibit relatively high LCOE values (0.265–0.335 $/kWh). However, the innovative multi-branch,

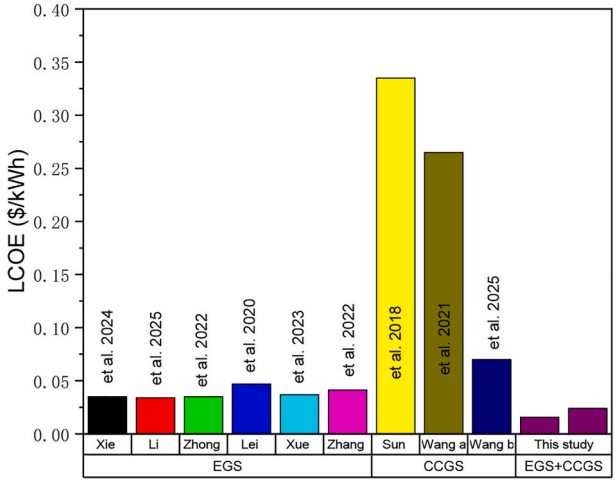


Fig. 28. Comparative chart of economic analysis under different geothermal development modes.

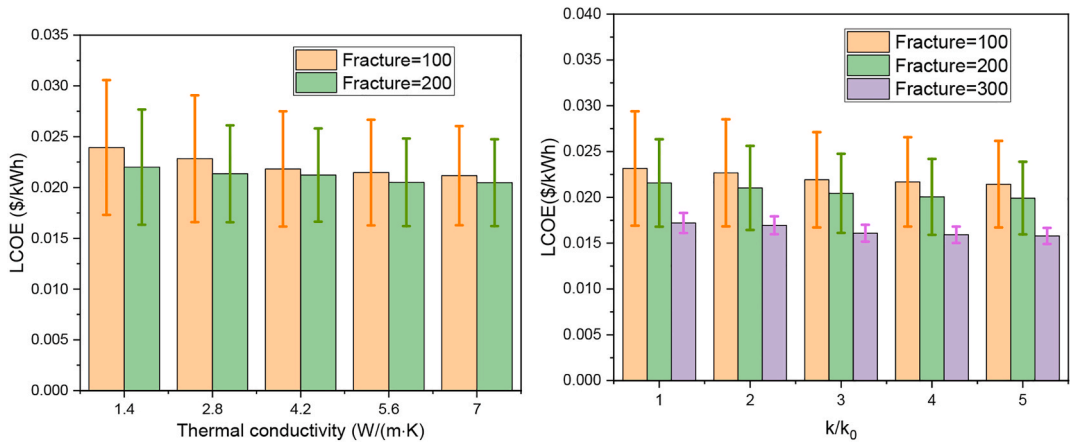


Fig. 27. Effect of the thermal conductivity and fracture permeability on LCOE.

Table 6
Economic analysis of different geothermal development methods.

System	Well layout	fracture	LCOE	sources
EGS	Pinnate well with	Parallel fracture	0.035 $/kWh	Xie et al. [37]
	Multi-vertical well	DFN fracture	0.0341 $/kWh	Li et al. [38]
	Dual well	DFN fracture	0.035 $/kWh	Zhong et al. [39]
	Three horizontal wells	Parallel fracture	0.047 $/kWh	Lei et al. [34]
	Three horizontal wells	Dual porosity method	0.037 $/kWh	Xue et al. [40]
	Two horizontal wells	Dual porosity method	0.0413 $/kWh	Zhang et al. [41]
CCGS	Single CHBHE	No fracture	0.265 $/kWh	Wang et al. [25]
	MLMB-CHBHE	No fracture	0.070 $/kWh	Wang et al. [42]
EGS-CCGS	Five horizontal wells	DFN fracture and good connectivity	0.0157 $/kWh	This study
		DFN fracture and poor connectivity	0.024 $/kWh	

multilayered coaxial well design reduces the cost substantially to 0.070 $/kWh. Notably, the EGS-CCGS hybrid system in this study demonstrates outstanding performance. By integrating both systems with DFN fracture connectivity technology, it achieves an LCOE of 0.0157–0.024 $/kWh.

5.3. Further work

The high viscosity of water (0.28-0.85 mPa s) limits its mobility in non-connected fractures, suppressing natural convection and reducing heat transfer to the CCGS system. Supercritical CO_2 ($scCO_2$; 31.1°C, 7.38 MPa) provides a viable alternative. Its low viscosity (0.02-0.08 mPa s), high diffusivity ($\sim 10^{-7}$ m^2/s), and low surface tension enable better penetration into poorly connected fractures [43,44], consistent with the permeability sensitivity results. Consequently, heat exchange between fractures and the rock matrix is enhanced, leading to more effective heat transport toward the wellbore and improved thermal extraction. Although the rock matrix is assumed to be impermeable in this model, fluid movement may still occur inside the disconnected fracture due to the difference in fluid density caused by temperature changes. Compared with water, CO2 has a lower viscosity, which enhances its natural circulation ability driven by buoyancy in these isolated fracture spaces, thereby expanding the heat affected range and improving the heat transfer efficiency.

In addition to the optimization method based on the physical model, the intelligent control strategy also provides new possibilities for improving the long-term operation performance of the coupled geothermal system. With the integration of hybrid reinforcement learning method [45] and uncertainty quantification approaches [46,47] for the EGS-CCGS physical model, dynamic optimization of injection flow and pressure parameters by using real-time operation data such as temperature and pressure can be achieved, so as to further improve the system operation stability and heat energy utilization efficiency.

Moreover, the thermo-hydro-mechanical-chemical (THMC) coupling effects will be further incorporated to evaluate the potential geomechanical risks and chemical contributions during long-term EGS-CCGS operation [48]. The impacts of high-pressure fluid injection and continuous reservoir cooling on stress redistribution, fracture evolution, permeability variation, and reservoir stability will be investigated to achieve a more comprehensive assessment of both heat extraction performance and operational safety [49,50].

6. Conclusions

In this paper, a novel geothermal system that combines EGS-CCGS systems is proposed. A mathematical model of the fluid flow and heat transfer in the fractures, reservoir matrix, and coaxial wellbore is established. Based on the results obtained in this work, the following conclusions are drawn:

(1) In the combined system, the degree of improvement of the CCGS geothermal system on the entire system is closely related to the connectivity of the fractures. When the connectivity is poor, the improvement rate is as high as 150%. In cases where the connectivity of the fractures is relatively better, the improvement rate of the CCGS system is as low as 20%.
(2) The optimal injection rates of the combined EGS-CCGS system are reported as 120 kg/s for the EGS injection and 25 kg/s for the CCGS injection.
(3) With 100-300 fractures, the heat extraction efficiency is proportional to the number of fractures. When the fracture number increases to 400, a fluid short circuit occurs in the fractured reservoir. This leads to a decrease in the heat extraction efficiency of the system.
(4) When the fracture connectivity is poor, the thermal conductivity of HDR has a significant impact on heat extraction efficiency, while the fracture permeability has a relatively minor effect. Conversely, the opposite effects are reported when the fracture connectivity is good.
(5) With fracture numbers ranging from 100 to 400, the LOCEs of the combined EGS-CCGS system are 0.022 $/kWh, 0.021 $/kWh, 0.017 $/kWh, and 0.016 $/kWh, and those of the EGS system are 0.031 $/kWh, 0.027 $/kWh, 0.018 $/kWh, and 0.16 $/kWh, under fracture numbers of 100, 200, 300, and 400, respectively. In this regard, the EGS system has a lower LCOE of 29%, 20%, 5%, and 0.6% as compared to those of the combined system proposed in this study.

CRediT authorship contribution statement

Guoying Wang: Writing – original draft, Investigation, Funding acquisition, Formal analysis, Conceptualization. **Guofeng Song:** Writing – review & editing, Validation, Investigation, Formal analysis. **Housheng Jia:** Resources, Project administration, Funding acquisition. **Hongwei Ma:** Writing – original draft, Investigation. **Lei Wang:** Resources, Investigation. **Norbert Klitzsch:** Writing – review & editing. **Shaowei Liu:** Software, Investigation. **Gan Feng:** Writing – review & editing. **Chuanliang Yan:** Formal analysis. **Zhazha Hu:** Writing – review & editing, Methodology.

Declaration of competing interest

The authors declare that they have no known competing financial interests or personal relationships that could have appeared to influence the work reported in this paper.

Acknowledgement

This study was funded by the National Natural Science Foundation of China (52104128, 52274078, 52374099), the National Key Research and Development Program of China (2019YFA0705501), and the Scientific and Technological Innovation Talents Project of Colleges and Universities in Henan Province (22HASTIT010).

Data availability

Data will be made available on request.

References

[1] Tester JW, Anderson BJ, Batchelor AS, Blackwell DD, DiPippo R, Drake EM, et al. Impact of enhanced geothermal systems on US energy supply in the twenty-first century. Philos Trans R Soc A Math Phys Eng Sci 2007;365(1853):1057–94.

[2] Pollack A, Mukerji T. Accounting for subsurface uncertainty in enhanced geothermal systems to make more robust techno-economic decisions. Appl Energy 2019;254:113666.

[3] Olasolo P, Juárez M, Morales M, Liarte I. Enhanced geothermal systems (EGS): a review. Renew Sustain Energy Rev 2016;56:133–44.

[4] Aliyu MD, Chen H-P. Sensitivity analysis of deep geothermal reservoir: effect of reservoir parameters on production temperature. Energy 2017;129:101–13.

[5] Shi Y, Zhang Y, Wang G, Zhang X, Song X, Cui Q, Wang G. Heat extraction mechanism in hot dry rock based on horizontal Wells with multi-stage fracturing. Energy 2026:140217.

[6] Falcone G, Liu X, Okech RR, Seyidov F, Teodoriu C. Assessment of deep geothermal energy exploitation methods: the need for novel single-well solutions. Energy 2018;160:54–63.

[7] Chamorro CR, García-Cuesta JL, Mondéjar ME, Pérez-Madrazo A. Enhanced geothermal systems in Europe: an estimation and comparison of the technical and sustainable potentials. Energy 2014;65:250–63.

[8] Wang Y, Li T, Chen Y, Ma G. Numerical analysis of heat mining and geological carbon sequestration in supercritical CO2 circulating enhanced geothermal systems inlayed with complex discrete fracture networks. Energy 2019;173:92–108.

[9] Timothy K. The EGS collab project: an intermediate-scale field test to address enhanced geothermal system challenges. Conference the EGS Collab Project: an intermediate-scale field test to address enhanced geothermal system challenges, vol. 205. EDP Sciences, p. 01002..

[10] Kneafsey T, Dobson P, Ajo-Franklin J, Guglielmi Y, Valladao C, Blankenship D, et al. EGS collab project: status, tests, and data. Conference EGS Collab Project: status, tests, and data. ARMA, p. ARMA-2019-04..

[11] Parker R. The rosemanowes HDR project 1983–1991. Geothermics 1999;28(4–5):603–15.

[12] Tenma N, Yamaguchi T, Zyvoloski G. The Hijiori hot dry rock test site, Japan: evaluation and optimization of heat extraction from a two-layered reservoir. Geothermics 2008;37(1):19–52.

[13] Lv Y, Yuan C, Gan Q, Li H, Zhu X. Analysis of heat transfer based on complex embedded discrete fracture network (EDFN) for field-scale EGS. Geothermics 2022;104:102463.

[14] Wang G, Song X, Shi Y, Yulong F, Yang R, Li J. Comparison of production characteristics of various coaxial closed-loop geothermal systems. Energy Convers Manag 2020;225:113437.

[15] Sun F, Yao Y, Li G, Li X. Geothermal energy development by circulating CO2 in a U-shaped closed loop geothermal system. Energy Convers Manag 2018;174:971–82.

[16] Wang G, Ma H, Liu S, Yang D, Xu X, Fu M, Jia H. Thermal power extraction from a deep, closed-loop, multi-level, multi-branch, U-shaped borehole heat exchanger geothermal system. Renew Energy 2022;198:894–906.

[17] Sharmin T, Khan NR, Akram MS, Ehsan MM. A state-of-the-art review on geothermal energy extraction, utilization, and improvement strategies: conventional, hybridized, and enhanced geothermal systems. Int J Thermofluids 2023;18:100323.

[18] Agson-Gani PH, Zueter AF, Xu M, Ghoreishi-Madiseh SA, Kurnia JC, Sasmito AP. Thermal and hydraulic analysis of a novel double-pipe geothermal heat exchanger with a controlled fractured zone at the well bottom. Appl Energy 2022;310:118407.

[19] Gao X, Zhang Y, Cheng Y, Huang Y, Deng H, Ma Y. A novel strategy utilizing local fracture networks to enhance CBHE heat extraction performance: a case study of the Songyuan geothermal field in China. Energy 2022;255:124536.

[20] Zhao Y, Feng Z, Feng Z, Yang D, Liang W. THM (Thermo-hydro-mechanical) coupled mathematical model of fractured media and numerical simulation of a 3D enhanced geothermal system at 573 K and buried depth 6000–7000 M. Energy 2015;82:193–205.

[21] Yao J, Zhang X, Sun Z, Huang Z, Liu J, Li Y, et al. Numerical simulation of the heat extraction in 3D-EGS with thermal-hydraulic-mechanical coupling method based on discrete fractures model. Geothermics 2018;74:19–34.

[22] Zhang J, Xie J, Liu X. Numerical evaluation of heat extraction for EGS with tree-shaped wells. Int J Heat Mass Tran 2019;134:296–310.

[23] Jin P, Hu Y, Shao J, Liu Z, Feng G, Song S. Influence of temperature on the structure of pore–fracture of sandstone. Rock Mech Rock Eng 2020;53(1):1–12.

[24] Kretzschmar H-J, Wagner W. Properties of water and steam: international steam tables based on the industrial formulation IAPWS-IF97. Springer Berlin; 2017.

[25] Wang G, Song X, Shi Y, Yang R, Yulong F, Zheng R, Li J. Heat extraction analysis of a novel multilateral-well coaxial closed-loop geothermal system. Renew Energy 2021;163:974–86.

[26] Gnielinski V. On heat transfer in tubes. Int J Heat Mass Tran 2013;63:134–40.

[27] Lauwerier H. The transport of heat in an oil layer caused by the injection of hot fluid. Appl Sci Res, Sect A 1955;5(2):145–50.

[28] Qu Z-q, Zhang W, Guo T-k. Influence of different fracture morphology on heat mining performance of enhanced geothermal systems based on COMSOL. Int J Hydrogen Energy 2017;42(29):18263–78.

[29] McLean M, Espinoza D, Ahmmed B. The impact of effective fractured rock mass properties on development of flow channeling in enhanced geothermal systems. Renew Energy 2024;237.

[30] Dai C, Li J, Shi Y, Zeng L, Lei H. An experiment on heat extraction from a deep geothermal well using a downhole coaxial open loop design. Appl Energy 2019;252:113447.

[31] Gao X, Zhang Y, Cheng Y, Yu Z, Hu Z, Huang Y. Heat extraction performance of fractured geothermal reservoirs considering aperture variability. Energy 2023;269:126806.

[32] Shi Y, Song X, Li J, Wang G, Zheng R, YuLong F. Numerical investigation on heat extraction performance of a multilateral-well enhanced geothermal system with a discrete fracture network. Fuel 2019;244:207–26.

[33] Cai X, Cai J, Liu Z, Deng Q, Wang S. Efficient heat extraction in enhanced geothermal systems reservoirs: from parameter coupling to structural optimization. Phys Fluids 2026;38(6).

[34] Lei Z, Zhang Y, Zhang S, Fu L, Hu Z, Yu Z, et al. Electricity generation from a three-horizontal-well enhanced geothermal system in the Qiabuqia geothermal field, China: slickwater fracturing treatments for different reservoir scenarios. Renew Energy 2020;145:65–83.

[35] Lukawski MZ, Anderson BJ, Augustine C, Capuano Jr LE, Beckers KF, Livesay B, Tester JW. Cost analysis of oil, gas, and geothermal well drilling. J Petrol Sci Eng 2014;118:1–14.

[36] Bloomfield K, Laney P. Estimating well costs for enhanced geothermal system applications. Idaho National Laboratory (INL); 2005.

[37] Xie J, Wang J. Numerical analysis and economic evaluation of pinnate horizontal well for supercritical CO2-based enhanced geothermal system. Geothermics 2024;116:102850.

[38] Li X, Wang J, Du C, Luo J, Gong W. Performance analysis of heat extraction in a multi-well EGS using a DFN-based modeling scheme. Appl Therm Eng 2025;269:125988.

[39] Zhong C, Xu T, Yuan Y, Feng B, Yu H. The feasibility of clean power generation from a novel dual-vertical-well enhanced geothermal system (EGS): a case study in the Gonghe Basin, China. J Clean Prod 2022;344:131109.

[40] Xue Z, Yao S, Ma H, Zhang C, Zhang K, Chen Z. Thermo-economic optimization of an enhanced geothermal system (EGS) based on machine learning and differential evolution algorithms. Fuel 2023;340:127569.

[41] Zhang Q, Yan X, Li Z. A mathematical framework for multiphase poromechanics in multiple porosity media. Comput Geotech 2022;146:104728.

[42] Wang G, Zhou F, Jia H, Klitzsch N, Feng G, Yan C, et al. Heat extraction performance of multi-level, multi-branch, closed loop coaxial horizontal borehole heat exchanger geothermal system. Appl Therm Eng 2025;269:126045.

[43] Shi Y, Cui Q, Song X, Li G, Wang G. Performances of a novel compressed CO2 energy storage and heat storage integration system using multi-stage hydraulic fractures of horizontal well in subsurface reservoirs. Renew Energy 2025;251:123396.

[44] Cui Q, Shi Y, Li S, Song X, Zhu B, Wang G, Peng J. Study on impacts of seasonal heat storage on CO2 geological sequestration and parameter optimization. Energy 2025:137698.

[45] Hazem ZB. A fuzzy-TD3 hybrid reinforcement learning framework for robust trajectory tracking of the Mitsubishi RV-2AJ robotic arm. Sci Rep 2026;16(1):12269.

[46] Song G, Geiger S, Voskov D, Abels HA, Vardon PJ. Scenario-based data assimilation framework to improve production estimates for geologically complex geothermal reservoirs. Geoenergy Sci Eng 2026;263:214490.

[47] Song G, Voskov D, Abels HA, Vardon PJ, Geiger S. Data-worth analysis using ensemble smoother with multiple data assimilation to constrain uncertainty in geothermal energy production from clastic fluvial reservoirs. Comput Geosci 2026;30(4):53.

[48] Song G, Shi Y, Xu F, Song X, Li G, Wang G, Lv Z. The magnitudes of multi-physics effects on geothermal reservoir characteristics during the production of enhanced geothermal system. J Clean Prod 2024;434:140070.

[49] Cai X, Ren X, Cai J, Ren J, Wang S. Balancing heat extraction and reservoir stability in enhanced geothermal system: mechanisms and synergistic evaluation based on thermo-hydro-mechanical coupling. Appl Therm Eng 2026:131568.

[50] Cai X, Xue R, Zhu J, Li J, Cai J, Wang S. Research on the natural compensation mechanism of reservoir temperature after geothermal extraction stops in open-loop geothermal systems based on heterogeneous reservoirs. Energy Build 2026:117822.